

# The dissolved oxygen ramp is immoral

Mariane Y. Schneider  
BIOMATH,  
Department of Data Analysis and Mathematical Modelling,  
Ghent University,  
Coupure Links 653, Ghent 9000, Belgium  
mariane.schneider@ugent.be

Elena Torfs  
modelEAU,  
Département de génie civil et de génie des eaux,  
Université Laval,  
pavillon Adrien-Pouliot, 1065, av. de la Médecine,  
Québec, G1V 0A6, Canada  
elena.torfs@gci.ulaval.ca

Juan Pablo Carbajal  
Institute for Energy Technology,  
OST Eastern Switzerland University of Applied Sciences,  
Oberseestrasse 10, 8640 Rapperswil, Switzerland  
juanpablo.carbajal@ost.ch

October 2024

## Abstract

On-site recovery and reuse allow saving dwindling water resources. However, for safe water reuse, it is essential to be able to guarantee a given water quality at all times. This is especially challenging for on-site water resource recovery facilities because sensors are unmaintained. Therefore, robust features for monitoring the treatment process are required. Here we present a method, i.e. [Dynamical Systems Analysis \(DSA\)](#), to explore models for informative features and systematically characterise these features. We exemplarily demonstrate the application of [DSA](#) to the [Activated Sludge Model 1](#), and explore a [ramp](#) feature in the dissolved oxygen signal used to detect full ammonium oxidation. Our findings show that the [ramp](#) feature is immoral, which means multiple state variables cause the observation of this feature, potentially leading to false positive detections. However, through [DSA](#), we show that the prediction accuracy is increased when the feature is selected based on a minimal value of the slope of the dissolved oxygen signal. The current analyses also provided further features that could increase the accuracy of the detection, in particular the concentration of autotrophic bacteria. We further highlight that the potential of [DSA](#) goes far beyond our results, including feature identification, calibration procedure and experimental design. We additionally provide all code open access and with examples so that readers can conduct their own analysis.

## Contents

<a href="#">1 Introduction</a>	<a href="#">2</a>
<a href="#">2 Results and Discussion</a>	<a href="#">5</a>
<a href="#">2.1 Model dependency graph</a>	<a href="#">5</a>
<a href="#">2.2 The dissolved oxygen ramp feature in detail</a>	<a href="#">5</a>
<a href="#">2.3 Identification of states leading to dissolved oxygen ramps</a>	<a href="#">7</a>
<a href="#">2.4 Immorality of the dissolved oxygen ramp</a>	<a href="#">8</a>
<a href="#">2.5 Ramp points distribution</a>	<a href="#">8</a>
<a href="#">2.6 Limitations</a>	<a href="#">9</a>
<a href="#">3 Conclusion</a>	<a href="#">9</a>

<b>4</b>	<b>Materials and methods</b>	<b>10</b>
4.1	Dissolved oxygen feature . . . . .	10
4.2	Model signal features . . . . .	10
4.3	Model structure . . . . .	11
4.4	Ramp contingency . . . . .	12
<b>A</b>	<b>Supplementary information</b>	<b>16</b>
A.1	Time derivatives . . . . .	16
A.1.1	Single state actuation . . . . .	17
<b>B</b>	<b>Ramp points curve</b>	<b>17</b>
B.1	Interpretability of the inflection point curve . . . . .	19
B.2	Symbols name . . . . .	19
B.3	ASM1 model . . . . .	19
<b>C</b>	<b>Causal diagram</b>	<b>24</b>
C.1	Ammonium depletion soft-sensor based on the dissolved oxygen ramp feature . . . . .	25

## Glossary

**ADM** Anaerobic Digestion Model. 3, 4, 9, 11

**ASM** Activated Sludge Model. 1, 3–11, 17, 24

**BSM** Benchmark Simulation Model. 4, 24

**DSA** Dynamical Systems Analysis. 1, 3–10, 25

**ODE** Ordinary Differential Equations. 3

**ramp** A time-based signal feature. It is defined as the signal’s non-saddle (non-zero first time derivative) inflection point (zero second time derivative).. 1, 2, 5–12, 17–20, 24, 25

**SBR** Sequencing Batch Reactor. 5, 10

## 1 Introduction

The impact of climate change on water cycles has a cascading effect on urban areas, agriculture, industry, and the natural environment, necessitating adaptation. A flexible, circular on-site infrastructure (Larsen et al., 2016; Rabaey et al., 2020), is a promising adaptation strategy. Furthermore, on-site plants may allow cost savings (Eggimann et al., 2018) and resource recovery (van Loosdrecht and Brdjanovic, 2014).

Monitoring and control is one decisive challenge inherent to on-site water and wastewater infrastructure. This is on the one hand attributable to the capital cost of sensors for target water quality variables creating the need for soft sensor (Haimi et al., 2013) development. On the other hand, monitoring is hampered by required sensor maintenance (Schneider et al., 2020). Most studies do not address the maintenance challenge even for on-site settings (e.g. Shyu et al., 2023). However, sensors expose a variety of often non-linear wearing effects such as damage, fouling, or deterioration (e.g. Alferes et al., 2024; Cecconi et al., 2020; Samuelsson et al., 2018; Ohmura et al., 2019) and sensor faults impact the treatment performance (Ivan and Zaccaria, 2024). The wearing effects are especially challenging to data-driven approaches, despite high accuracy results (e.g. Li et al., 2023), as they might be outside the training dataset. Consequently, sensors should either be installed in an environment where nearly no maintenance is required, for example, a chlorination tank (Reynaert et al., 2023) or features (Schneider et al., 2019) and control patterns (Thürlimann et al., 2019) need to be by design robust to the specific sensor wearing effects.

Schneider et al. (2019) directly compared a soft sensor to predict complete ammonia oxidation using a ramp feature (i.e. a non-saddle inflection point, see "Ramp" in fig. 6) in the dissolved oxygen signal based on data from maintained and unmaintained sensors. The ammonium-depletion detection based on the ramp feature is quite robust to inaccuracies due to wearing of the physical sensor. Nevertheless, three time-consuming sampling campaigns and extensive simulations with existing mechanistic models revealed at least two alternative causes for the dissolved-oxygen ramp feature i.e. the aeration pattern and alkalinity limitation. Additionally, a short solids retention time (Schneider et al., 2020) made the ramp disappear for ammonium concentrations below an arbitrary threshold. Hence, designing robust soft sensors is constrained by our ability to systematically explore the causes of the feature, e.g. due to the plethora of state combinations that can lead to it. Moreover, the presence of alternative causes for the feature (see the supplementary information sec. C) poses a risk of erroneous soft

sensor predictions, potentially affecting human and environmental health. To avoid these undesired effects, a systematic identification of the alternative causes and the analysis of the plausibility of their occurrence is required.

For complex systems such as human brains, global weather, or biochemical wastewater treatment processes, understanding the functional architecture to define effective, rigorous, principled, and general methods is important, yet remains a challenge (Rosas et al., 2024). To find such a method, we systematically analyse sets of [Ordinary Differential Equations \(ODE\)](#) using an approach that we call [DSA](#) (see [Strogatz, 2024](#), for a joyful introduction). The approach aims at understanding a set of [ODEs](#) without integrating them, usually leading to efficient workflows and adding a novel perspective to problem-solving. [DSA](#) encompasses techniques for characterising stability and bifurcations (cf. tipping points), and it allows screening any dynamic model for a plethora of features and engineering features useful for monitoring and control. In other fields, such as robotics, [DSA](#) is frequently employed ([Akashi et al., 2024](#); [Carbajal et al., 2022](#); [Caluwaerts and Carbajal, 2015](#), e.g.) to gain mathematical insights into the engineering problem to solve, which more often than not lead to novel solutions. In climate science, [DSA](#) has been used to predict abrupt changes like tipping points ([Bathiany et al., 2016](#)). [DSA](#) also provides an alternative perspective into model calibration ([Haller, 2023](#), ch. 1), which focuses on validating structural features of the model with experimental data, as opposed to the more conventional approach of matching time series.

In wastewater treatment, [DSA](#) remains an uncommon approach. When [DSA](#) is employed, it is frequently referred to with ambiguous terms like "analysis", which hinders identifying relevant studies. We, therefore, believe that a review on [DSA](#) applied in biochemical treatment and recovery processes of wastewater and similar streams is timely, especially to the popular [Activated Sludge Model \(ASM\)](#) ([Henze et al., 2000](#)) and [Anaerobic Digestion Model \(ADM\)](#) ([Batstone et al., 2002](#)). Hence, we provide a brief review in tab. 1.

Reference	Model	DSA outcome	Implication/application
Vanrolleghem (1994)	ASM1 and solid flux sedimentation model	Degradation and settling should be considered for control design	Improved control design
Grognard and Bernard (2006)	Two-population model for anaerobic process	Stability analysis with non-trivial solutions	How to avoid instability e.g. acidification
Shen et al. (2007)	Anaerobic digestion	Identified three stable points under usual operation, and a saddle-node bifurcation	Find stable operating conditions
Nelson and Sidhu (2009)	ASM1	Identified two branch points	Determine optimal residence time
Volcke et al. (2010)	Two-step biological conversion system	Steady state multiplicity was identified	Experimental design
Benyahia et al. (2012)	Two-step ADM	Bifurcation and stability analysis	Experimental design for monitoring strategy for soluble microbial products
Bornhöft et al. (2013)	ADM1	Bifurcation analysis	Model selection: Impact of model simplification
Dionisi et al. (2016)	Two-population model in a batch process	Stability analysis	Accelerate calculations to reach steady state
Wade and Wolkowicz (2021)	Impulsive annamox	Bifurcation analysis	Predict wash-out of nitrite-oxidising bacteria
Neto et al. (2022)	Benchmark Simulation Model1 (BSM)	Structural controllability and observability	Stability, controllability and observability
Sampaio et al. (2022)	ASM1-based with greenhouse-gas emissions, two-step nitrification, four-step denitrification and 10-layer settling	Structural analysis	Show if full-state controllable and observable for greenhouse gas emissions

Table 1: Literature review on DSA in anaerobic digestion and activated sludge modelling for wastewater treatment.

These successful examples from the water sector indicate the **DSA**'s value for analysis of steady-states and stability analysis contributing to experimental design and identifying regions of optimal operation, control, or observability. However, the use in other fields shows, that the potential of **DSA** is far from exhausted in the water sector. We assess that systematic detection of information-rich system dynamics (i.e. features) merits further attention, with applications in for example feature-based model calibration and feature engineering for soft-sensor development, the latter being the primary focus of the current study.

## 2 Results and Discussion

Herein, we use **DSA** to showcase how to analyse a biochemical model for features to be used in soft sensors. To model the activated sludge process we used the mass balance-corrected version of **ASM1** (Henze et al., 1987) by Hauduc et al. (2010). We exemplify the use of **DSA** for feature engineering by systematically investigating factors affecting the **ramp** feature in the dissolved oxygen signal in an **Sequencing Batch Reactor (SBR)** to predict the effluent ammonium concentration. The current work complements previous data-driven, mechanistic, or hybrid feature-learning approaches (Schneider et al., 2022) on a process familiar to the authors to introduce and discuss **DSA** as a potential standard procedure for soft-sensor development.

### 2.1 Model dependency graph

A worthwhile first step to get an overview before doing a **DSA** is a visual inspection of the dependencies. The dependency graph implies causation from the relations between states defined in the analysed model. Figure 1 shows the dependence graph of the 14 states of the mass-balance-corrected **ASM1** Hauduc et al. (2010). The many circular dependencies reflect the high complexity of the system. Furthermore, all processes follow the pattern state→rate→state, which hints at the specific model structure presented in sec. 2.3. By looking at the arrows and their direction, we can identify that five of these states do not affect the dynamics of the other states, of which two are uncoupled (no children or parents in the graph, i.e.  $X_{nb,in}$ ,  $S_{nb}$ ), and three are measurements (no children, i.e.  $X_{nb,e}$ ,  $S_{N2}$ ,  $S_{alk}$ ). Therefore, the dynamics of **ASM1** are determined by the following nine states (in brackets is the notation by Henze et al. (1987)):

- $S_b$  Soluble biodegradable organics (SS)
- $X_{cb}$  Particulate and colloidal biodegradable organics (XS)
- $X_h$  Ordinary heterotrophic organisms (XBH)
- $X_a$  Autotrophic nitrifying organisms (NH4+ to NO3-, XBA)
- $S_{O2}$  Dissolved oxygen (SO)
- $S_{NOx}$  Nitrate and nitrite (NO3 + NO2) (considered to be NO3 only for stoichiometry, SNO)
- $S_{NHx}$  Ammonia (NH4 + NH3) (SNH)
- $S_{bN}$  Soluble biodegradable organic N (SND)
- $X_{cbN}$  Particulate and colloidal biodegradable organic N (XND)

### 2.2 The dissolved oxygen ramp feature in detail

To illustrate the traditional way of finding inflection points (i.e. ramp features), we show in fig. 2 the time-series of the states of **ASM1** generated by one set of initial conditions. With  $S_{O2}$  and  $S_{NHx}$  in the top panel true and false positive **ramp** features can be identified in this single batch run. The vertical lines represent time instances where the conditions of a ramp in the oxygen signal (defined in eqs. (9)-(10)) are satisfied.

The first **ramp** in the  $S_{O2}$  signal is particularly interesting. If the soft sensor does not identify this ramp correctly to stop the treatment process, the ammonium concentration starts rising. The relevant process is the ammonification during the decay of heterotrophic bacteria in the absence of sufficient autotrophic bacteria. The second **ramp** is a false positive one. The third **ramp** is what we generally would expect in a biochemical treatment process that recovers wastewater batch-wise. Remarkable is also that the two true positive **ramps** have a much steeper slope than the false positive one. The first objective of the present work is to use **DSA** to efficiently screen for potential causes of false positives in the **ramp** feature. In a further objective, the potential of **DSA** to make the **ramp** feature more robust is explored.

Formally, **ramps** are zeros of the second time derivative in which the first derivative is positive (i.e. non-saddle inflection point). The locus<sup>1</sup> of **ramps** can be described mathematically by:

$$\text{ramps} := \{t : \dot{x}(t) > 0 \wedge \ddot{x} = 0\} \quad (1)$$

where the signal is given by  $x(t)$  and the dotted symbols represent time derivatives, and the wedge ( $\wedge$ ) is the logical conjunction (and) symbol, meaning that both criteria need to be fulfilled simultaneously.

<sup>1</sup>set of all points that satisfies the specified conditions

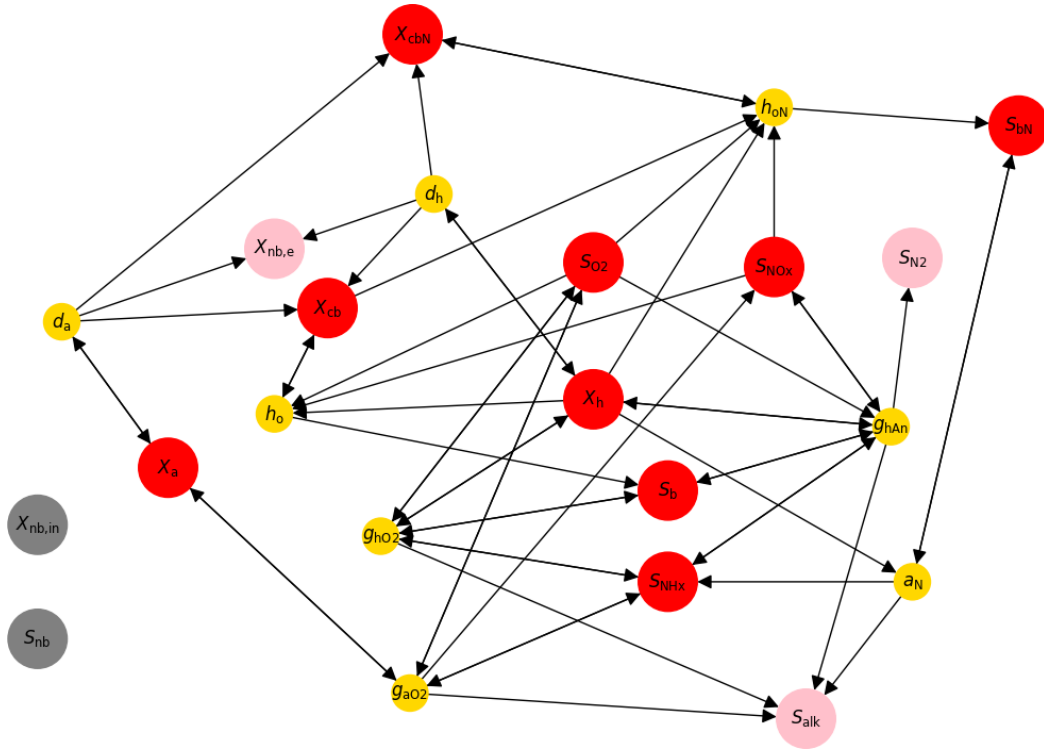


Figure 1: ASM1 state dependency graph. The graph depicts the interactions between the states in the model. States (larger nodes) affect rates (smaller nodes), which in turn affect the states through their time derivative. The arrows indicate which states and rates affect each other. Pink nodes with no child are measurements which do not impact other states. Grey nodes with neither parent nor child are uncoupled (i.e. the non-biodegradable organics,  $S_{nb}$ , and particulate non-biodegradable organics from the influent,  $X_{nb,in}$ ). The red nodes are the potential alternative causes for the **ramp** feature that would lead to a false prediction of the target variable.

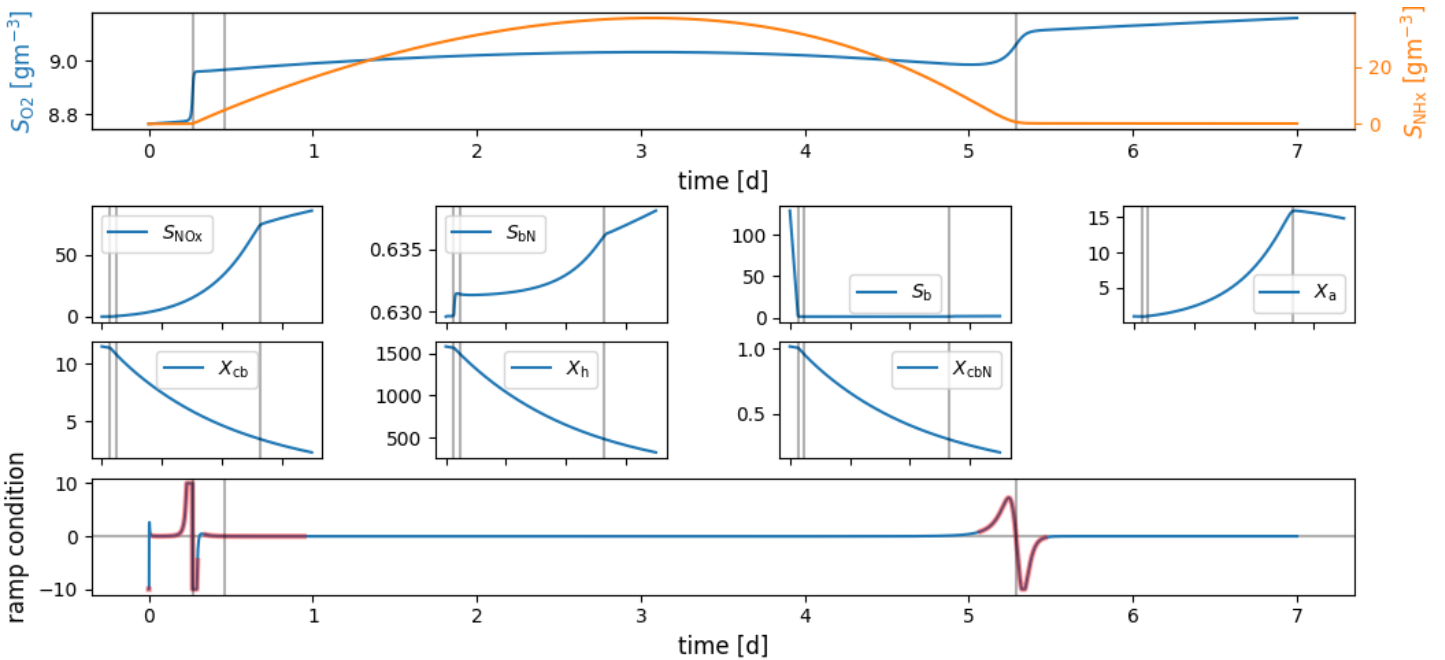


Figure 2: The top panel shows the  $S_{O_2}$  and the  $S_{NH_x}$  signals. The **ramp** time instances are marked on all panels as vertical lines and the time intervals on the x-axes are the same. The second **ramp** is a false positive for the effluent ammonium concentration estimation, the third one is a true positive feature, and the first one is a true positive that is not caused by the ammonium reaching a concentration below the threshold at the **ramp**-occurrence time, but the ammonium is already low before. By looking at the other panels, potential causes for the **ramp** features can be visually detected. The plots are for one single set of initial conditions. Each of these three **ramp** observations corresponds with one point on an inflection point curve. The time series are displayed here to display the **ramp** features. However, these time series will not be simulated in the DSA to obtain the inflection point curves. The units of all state variables are  $gm^{-3}$ .

### 2.3 Identification of states leading to dissolved oxygen ramps

To identify the states that lead to a **ramp** feature in the dissolved oxygen signal (represented by the state  $S_{O_2}$  in the **ASM** family), we need to compute the second time derivative of this state (i.e.  $\ddot{S}_{O_2}$ ), see eq. (13). This derivative can be computed directly from the model equations without simulating the full set of equations to generate a signal, a fact that makes **DSA** a particularly powerful and computationally efficient method. This computation can be done for any model structure, but for the **ASM** family the computations are simplified thanks to the structure of the model that can for example be identified from fig. 1:

$$\dot{\boldsymbol{x}} = \mathbf{M} \boldsymbol{r}(\boldsymbol{x}) + \boldsymbol{z} \quad (2)$$

$$\ddot{\boldsymbol{x}} = \mathbf{M} \dot{\boldsymbol{r}} + \dot{\boldsymbol{z}} = \mathbf{M} \mathbf{J}_r \dot{\boldsymbol{x}} + \dot{\boldsymbol{z}} \quad (3)$$

where we used boldface, e.g.  $\boldsymbol{x}$ , for vectors, and capital typewriter font, e.g.  $\mathbf{M}$  for matrices. In eq. (2),  $\boldsymbol{x}$  is the vector of states of the model. The states are then transformed via the mapping  $\boldsymbol{r}(\boldsymbol{x})$ , into a new vector, which herein we will call *rates* vector. The matrix  $\mathbf{M}$ , such as the stoichiometric matrix **Gujer and Henze (1991)**, combines the rates to produce the time derivatives of the states. The additional term ( $\boldsymbol{z}$ ) in eq. (2) represents the *actuation* on the states of the system. More details and explanations are given in sec. 4.3. Therefore, if the autonomous part of the model,  $\mathbf{M}$  and  $\boldsymbol{r}(\boldsymbol{x})$ , are given in tabular form, we can evaluate eqs. (2) and (3) directly, which allows to analyse any features based on time derivatives of the model states in this way.

Applying these formulae to **ASM1** (given in supplementary information B.3), we obtain equations for the first and second time derivative of the dissolved-oxygen state ( $S_{O_2}$ ). For the first derivative we get:

$$\dot{S}_{O_2} = m_{S_{O_2} g_{aO_2}} g_{aO_2}(S_{NHx}, S_{O_2}, X_a) + m_{S_{O_2} g_{hO_2}} g_{hO_2}(S_{NHx}, S_{O_2}, S_b, X_h) + z_{O_2} \quad (4)$$

$$m_{S_{O_2} g_{aO_2}} := \frac{\gamma_a + \iota_{COD,NO_3}}{\gamma_a} \quad m_{S_{O_2} g_{hO_2}} := \frac{\gamma_h - 1}{\gamma_h} \quad (5)$$

$$g_{aO_2}(S_{NHx}, S_{O_2}, X_a) := \mu_{\max,a} X_a \frac{S_{NHx} S_{O_2}}{(S_{NHx} + \kappa_{NHx,a})(S_{O_2} + \kappa_{O_2,a})} \quad (6)$$

$$g_{hO_2}(S_{NHx}, S_{O_2}, S_b, X_h) := \mu_{\max,h} X_h \frac{S_{NHx} S_{O_2} S_b}{(S_{NHx} + \kappa_{NHx,h})(S_{O_2} + \kappa_{O_2,h})(S_b + \kappa_b)} \quad (7)$$

Since the biological activity of heterotrophic and autotrophic bacteria consumes dissolved oxygen, the first two terms are always non-positive. The signs of  $m_{S_{O_2} g_{aO_2}}$  and  $m_{S_{O_2} g_{hO_2}}$  are determined by the coefficients in eq. (5), and for plausible values of  $\gamma_a$  and  $\gamma_h$  (see tab. 4), these signs are negative.

In the equations above we explicitly show the dependency of the rates (states in parentheses) that we extracted from the model equations. We omit them in the formulae for the second derivative:

$$\begin{aligned} \ddot{S}_{O_2} = & \dot{S}_{NHx} \partial_{S_{NHx}} (g_{aO_2} m_{S_{O_2} g_{aO_2}} + g_{hO_2} m_{S_{O_2} g_{hO_2}}) \\ & + \dot{S}_{O_2} \partial_{S_{O_2}} (g_{aO_2} m_{S_{O_2} g_{aO_2}} + g_{hO_2} m_{S_{O_2} g_{hO_2}}) \\ & + \dot{S}_b \partial_{S_b} g_{hO_2} m_{S_{O_2} g_{hO_2}} + \dot{X}_a \partial_{X_a} g_{aO_2} m_{S_{O_2} g_{aO_2}} + \dot{X}_h \partial_{X_h} g_{hO_2} m_{S_{O_2} g_{hO_2}} \\ & + z_{O_2} \partial_{S_{O_2}} (g_{aO_2} m_{S_{O_2} g_{aO_2}} + g_{hO_2} m_{S_{O_2} g_{hO_2}}) + \dot{z}_{O_2} \end{aligned} \quad (8)$$

The conditions for the **ramp** (section 4.2) read:

$$\dot{S}_{O_2} > 0 \quad (9)$$

$$\ddot{S}_{O_2} = 0 \quad (10)$$

The first condition for a **ramp**, eq. (9), requires the time derivative in this equation to be positive. This expresses the fact that the rate at which oxygen is transferred to the liquid phase ( $z_{O_2}$ ) needs to be bigger than the oxygen uptake rate by the bacteria, as there cannot be more oxygen consumed than is present. Therefore, in **ASM1** the dissolved oxygen **ramp** is a feature that can only be generated with a source of dissolved oxygen (aeration) as otherwise eq. (9) cannot be fulfilled. This underlines the role of aeration for the detection and robustness of the **ramp** feature, which in a different context, was observed in a real-world case in (**Schneider et al., 2020**).

Using **DSA** shows that the conditions (9) and (10) depend on other states besides  $S_{NHx}$  and  $S_{O_2}$ , i.e.  $S_{NOx}$ ,  $S_{bN}$ ,  $S_b$ ,  $X_a$ ,  $X_{cb}$ ,  $X_h$ . So, even if we kept  $S_{NHx}$  constant at a value above the prediction threshold for a full ammonium depletion, changes to these other states could generate a **ramp** that is not due to a  $S_{NHx}$  below this threshold. This can potentially lead to false positive predictions with a **ramp**-based soft sensor.

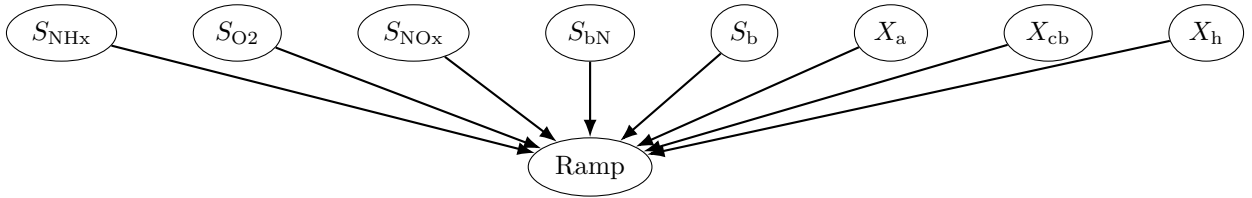


Figure 3: Causes of the  $S_{O_2}$  **ramp** feature. Obtained from the variables in eq. (8). Several V-structures are identified from the causal relations.

## 2.4 Immorality of the dissolved oxygen ramp

From the nine states in the dependency graph (1), **DSA** shows that only eight are actual causes of a **ramp**,  $X_{cbN}$  is not a cause. These eight states form several V-structures within the causal diagram of the **ramp** feature in fig. 3; know as *immoralities* (Pearl and Mackenzie, 2018). The states (parents) in a V-structure, will be associated (correlated) when data is selected conditional on the presence of the feature (child). These correlations can be exploited by a data-driven machine learning model to infer difficult-to-monitor states, e.g.  $S_{NHx}$  from  $S_{O_2}$ , or to alleviate an effluent ammonium prediction task. However, since pure data-driven approaches are limited to exploiting correlations without guaranteeing causality; adding causal relations, as we do here, can enhance the performance and information extracted from the method, e.g. to include root cause analysis.

**DSA** allows the systematic evaluation of conditions that lead to a ramp in a search process by sampling the states independently to determine the causes (parents) of the ramp feature, see fig. 3. This is illustrated in fig. 4a which shows all ramps found on the  $(S_{O_2}, S_{NHx})$  plane for 10,000 uniformly distributed random values of all the other six states that can cause **ramps** (see section B for explanations on how to read these curves). Each line is a 0-level set curve of eq. (10) that satisfies eq. (9). In this figure, we can see that many of these **ramps** are below an arbitrary threshold of  $1 \text{ g m}^{-3} S_{NHx-N}$ . All the ramps below the threshold would lead to the correct conclusion that the ammonium oxidation process is complete (true positive), hence the feature is informative. However, many other ramps are clearly above the threshold, and would lead to an erroneous conclusion (false positive).

Similarly, fig. 4b shows all ramps found on the  $(S_{O_2}, X_a)$  plane for the autotrophic bacteria that are responsible for the removal of nitrogen compounds such as ammonium. We have sampled values of  $S_{NHx}$  above the arbitrary threshold, between  $1 \text{ g m}^{-3}$  to  $200 \text{ g m}^{-3}$ . For all other states, we used the same ranges as before. Hence, only false positive **ramps** are shown in this plot. This allows us to evaluate causes of false positive results and identify measures to increase accuracy. The pattern clearly shows that a minimum concentration of  $X_a$  could drastically reduce the false positive results.

In summary, fig. 4a and fig. 4b illustrate how **DSA** can be used to systematically scan a feature space for the occurrence of features and their causes. Analysing the equations allows us to identify causal relations, which is very different from checking data for correlation. For an extended discussion of these results concerning experimental work in (Schneider et al., 2020, 2019) see sec. C.1.

## 2.5 Ramp points distribution

Figure 5 shows the distribution of states that cause a **ramp** feature (satisfy eqs. (9)- (10)). Blue and orange dots indicate effluent ammonium concentrations below and above an arbitrary threshold (T), respectively. Blue dots are thus true positives for the ammonium soft sensor and orange dots represent false positives. The plot also shows the value of the dissolved oxygen time derivative at these points. We observed in fig. 2 that true ramps are associated with higher derivatives than false ramps. The top right panel of fig. 5 ( $S_{NHx}$  vs  $\dot{S}_{O_2}$ ) supports this observation, as almost no false **ramps** are found above dissolved oxygen time derivatives of  $400 \text{ g m}^{-3} \text{ d}^{-1}$ . Therefore, using time derivative information (slope in a time series plot) together with the detection of **ramps** constitutes a more accurate feature.

This observation also provides a plausible explanation for the improved accuracy of an ammonium depletion classifier when slope information was included because without it the feature was not informative (Schneider et al., 2019, 2020). **ASM1** already captures this relation, despite missing processes and its relative simplicity compared to other activated sludge models. Identifying such a slope dependence shows that for the **ramp**-feature design **ASM1** is structurally useful. Hence, we demonstrate how **DSA** can be used for a structural verification of a model.

In the top right panel of fig. 5 we further see that if the false positives are eliminated by choosing a minimal slope and rejecting all **ramps** below the chosen slope (e.g.  $< 400 \text{ g m}^{-3} \text{ d}^{-1}$ ) a lot of false negatives would occur. The coloured shaded regions for different levels of  $X_a$  indicate that these levels could be used to lower the slope tolerance, and, therefore, reduce the false negatives. Hence, finding a feature to predict  $X_a$  would further increase the accuracy of the ramp-based soft sensor.

Further patterns can be recognised in fig. 5, such as if  $S_{bN}$  is above approximately  $7 \text{ g m}^{-3}$  there are no correct predictions possible anymore. It is reasonable to think that if the soluble biodegradable organic nitrogen is high, too much ammonium is formed, and its concentration drop is limited. The experimental confirmation of this discovery is part of future work. Furthermore, observing multiple additional patterns to the ones discussed in this article shows a great potential for future

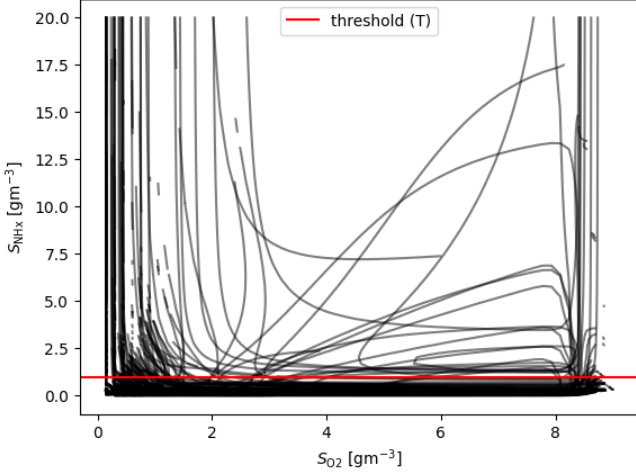
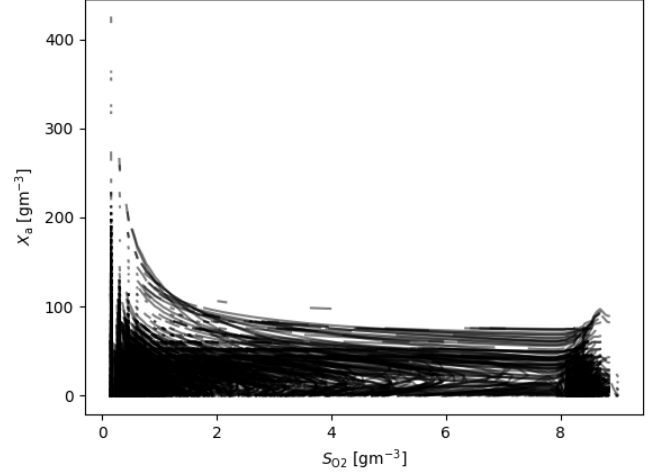
(a) Locus of all ramps in the (O<sub>2</sub>, Y) plane for  $S_{\text{NH}_x}$ .(b) Locus of false positive ramps in the (O<sub>2</sub>, Y) plane for  $X_a$ .

Figure 4: Inflection point curves in the respective (O<sub>2</sub>, Y) plane for two state variables. The Lines show the combinations of O<sub>2</sub> and Y concentrations that lead to a ramp feature. The simulation was done for 10,000 different initial conditions for each panel. The darker the area, the more overlapping inflection points are in the region. The ammonium concentrations for b) were restricted so that the panel only shows false positive ramps.

studies, e.g., to further improve the soft sensor with an estimate  $X_a$  or to identify an early warning feature for loss of nitrifying biomass.

Herein, we demonstrated how DSA can be used to improve the feature, e.g. by adding further constraints on a feature such as with the slope of  $S_{\text{O}_2}$ . DSA could also be used to discover feature sets from signals of other sensors than dissolved oxygen that further improve the accuracy and robustness of an ammonium-depletion soft sensor or soft sensors for different quantities of interest.

We provide all the code under a GNU free public license in Carbajal and Schneider (2024), hence readers can adapt it to their own analyses and for different models, as long as they have the structure described in eq. (3).

## 2.6 Limitations

There is another known state variable that could cause a ramp: the alkalinity (Al-Ghusain et al., 1994), which does not influence other states in the definition of ASM1. No DSA performed on this model will inform us of the influence of alkalinity. This is because DSA is applied to a specific model, and is restricted by the model's structure. The presented method for DSA can be applied to other models such as ASM3 which would allow us to assess the relationship between alkalinity and the ramp feature. However, in the present work, it was decided to develop a proof of concept of the method based on ASM1 as this is still the most commonly used model in the ASM family.

## 3 Conclusion

1. We used DSA to systematically evaluate all the mathematically possible solutions leading to a ramp feature in the oxygen signal in ASM1. The dissolved oxygen ramp is clearly immoral, which means that not only a low ( $S_{\text{NH}_x}$ ), hence an ammonium depletion, causes the ramp feature, but also eight alternative causes, i.e.  $S_{\text{O}_2}$ ,  $S_{\text{NO}_x}$ ,  $S_{\text{bN}}$ ,  $S_{\text{b}}$ ,  $X_a$ ,  $X_{\text{cb}}$ ,  $X_{\text{h}}$ ,  $X_{\text{cbN}}$ .
2. We could identify with DSA that the slope of the dissolved oxygen at the locus of the ramp is relevant and can increase the accuracy of the ramp feature.
3. Many models (e.g. ASM family or ADM1) follow the same structure which means that the formulae presented here can be applied "as-is" for a plethora of models in the water and resource recovery domain.
4. The same analysis could be done with extrema or other features based on time derivatives of the model's signals and is relevant for any under-actuated, heavily natural system because they share the underlying challenges of complex, only partially observable systems.

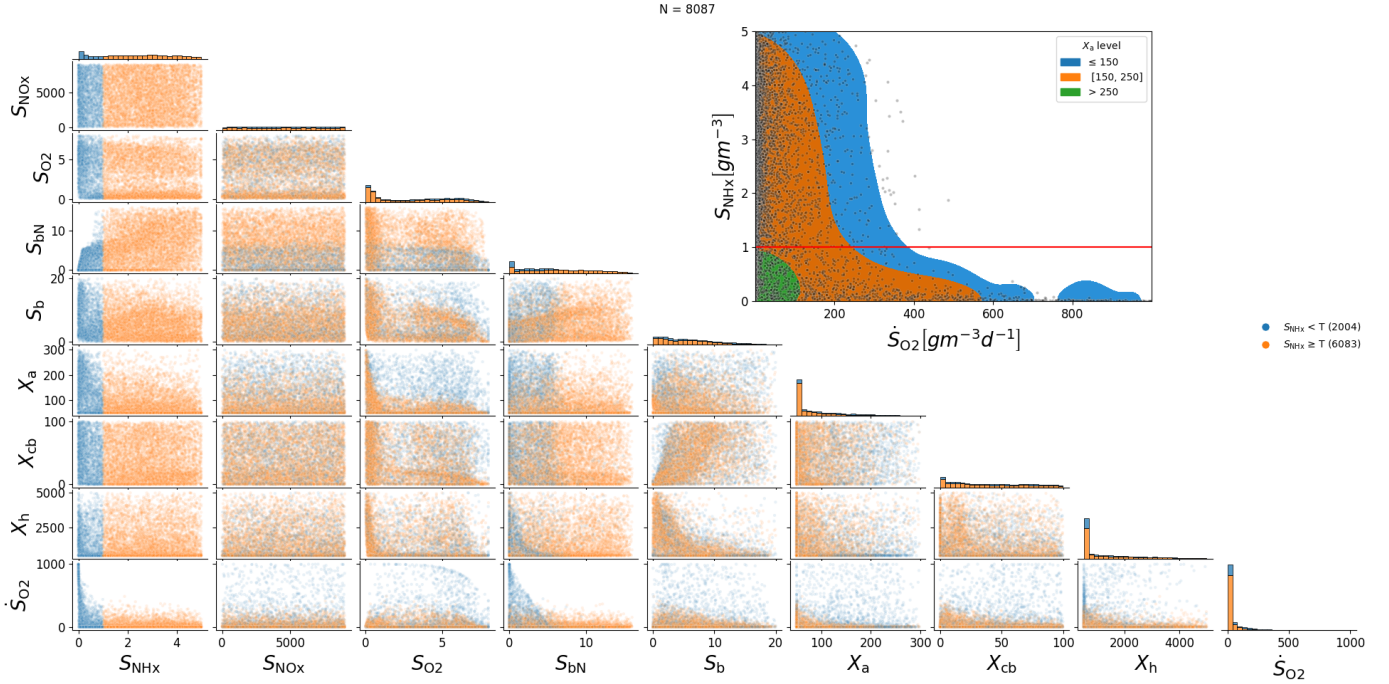


Figure 5: **ASM1** ramp points distribution. Distribution of states fulfilling the ramp conditions (9) and (10). The points are colored by whether the value of  $S_{\text{NHx}}$  is above or below an arbitrary threshold ( $T$ ). The number of samples ( $N$ ) in each category is shown in the legend. The panels on the diagonal always show the density of points. The bottom row of the panels shows the value of the dissolved oxygen time derivative (ramp’s slope). The top-right panel shows the relation between the ramp’s slope and the ammonium concentration. The coloured regions on that panel show the level of  $X_a$ , illustrating a further correlation that can be exploited for increasing the accuracy of full ammonium depletion detection.

## 4 Materials and methods

### 4.1 Dissolved oxygen feature

As introduced in section 1, a feature can be used to monitor a biochemical wastewater treatment process. From the two measurement signals pH and dissolved oxygen from a previous study (Schneider et al., 2019), we here chose the latter, as  $S_{\text{O}_2}$  is a state in the **ASM1** while pH is not a state variable in any of the **ASM** models. This allowed us to start with a model with a small number (eight) of equations to implement. The feature of the dissolved oxygen is a **ramp** (see fig. 6) that can be used to predict the ammonium ( $S_{\text{NHx}}$ ) effluent concentration. Olsson and Andrews (1978) describe the ramp feature for a plug flow reactor, hence w.r.t. the location. Following the same principle in our study, we use an **SBR**, thus the ramp is w.r.t. time, i.e. whenever an inflection point is observed during the aeration phase, we assume that the ammonium is fully oxidised so the ammonium nitrogen is below or equal to an arbitrary threshold of  $1 \text{ g m}^{-3}$  (Schneider et al., 2020). If there is no ramp feature the effluent ammonium concentration is estimated to be above  $1 \text{ g m}^{-3}$ . For this prediction to be accurate and robust there should be no other state than an ammonium concentration below or equal to  $1 \text{ g m}^{-3}$  leading to the **ramp** feature. First, we obtain all the mathematically possible solutions for a **ramp** feature in **ASM1** with **DSA**. See 4.2 for a detailed description of how we obtained these solutions. Next, we further constrain these mathematically possible solutions to the physically plausible ones by restricting them to only positive states. Restrictions were that concentrations cannot be negative and the setting of a wide, yet feasible range for all state variables. See tabs. 5-7 in the supplementary information for ranges that are reported in the literature, which we consulted to restrict the phase space of the state variables.

### 4.2 Model signal features

We are concerned with computing signal features based on the signal’s derivatives w.r.t. time (time derivatives). Figure 6 shows two examples of such features: a valley that is a minimum extreme point and a **ramp**. Extrema are zeros of the signal’s first time derivative, and **ramps** are zeros of the second time derivative in which the first derivative is positive (i.e. non-saddle inflection point). The locus<sup>2</sup> of **ramps** can be described mathematically by (1).

Eq. (1) can be used with signals that are differentiable twice. Also, we exclude saddle-points by requiring that the first time derivative is positive. The definition of **ramp** includes the concavity changing points of sigmoid functions like the hyperbolic tangent (as shown in fig. 6) and points at which the signal looks locally like a straight line (i.e. proportional to time), even if its concavity does not change sign.

<sup>2</sup>set of all points that satisfies the specified conditions

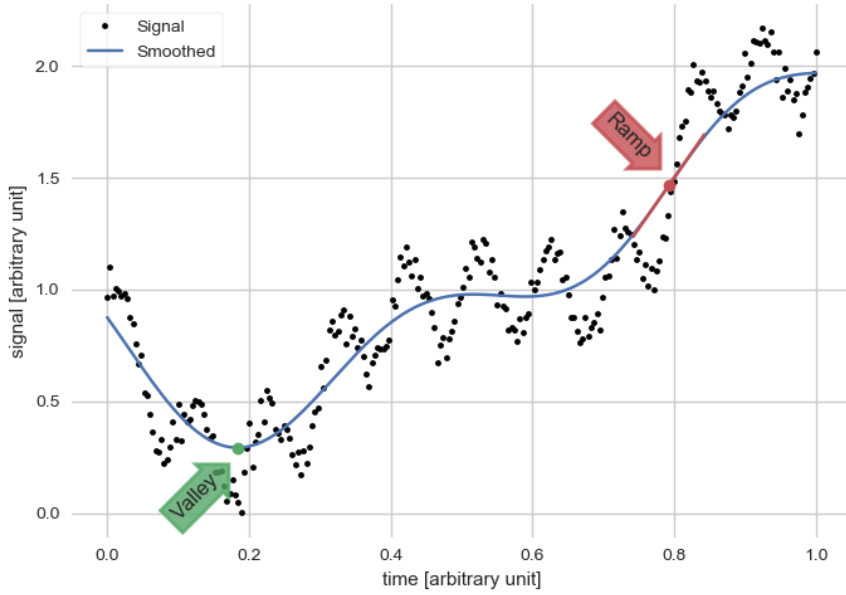


Figure 6: Illustration of two different features based on time derivatives of a signal. An extrema (valley) and a non-saddle inflection point (ramp). The latter we use in this article. The figure is created with [Carbajal and Schneider \(2019\)](#).

Therefore, by obtaining an expression of the first and second time derivatives of the signal directly from the model, we can compute the locus of all [ramps](#) without solving the full differential equations or modelling time series.

### 4.3 Model structure

We apply our approach to models with the following structure:

$$\dot{\mathbf{x}} := \mathbf{M} \mathbf{r}(\mathbf{x}) + \mathbf{z} \quad (11)$$

$$\mathbf{y} := \mathbf{h}(\mathbf{x}) \quad (12)$$

where we used boldface, e.g.  $\mathbf{x}$ , for vectors, and capital typewriter font, e.g.  $\mathbf{M}$  for matrices. In eq. (11),  $\mathbf{x}$  is the vector of states of the model, which herein we take to be a real column matrix, i.e.  $\mathbf{x} \in \mathbb{R}^{N \times 1}$  ( $N$  is the number of states, e.g.  $N = 13$  in the original [ASM1](#), [Henze et al. \(1987\)](#)). The states are then transformed via the mapping  $\mathbf{r}(\mathbf{x})$ , into a new vector, which herein we will call *rates* vector and, by slight abuse of notation, denote also  $\mathbf{r}$ . This transformation might not preserve the dimension, so the resulting rates vector might have a different dimension  $\mathbf{r}(\mathbf{x}) \in \mathbb{R}^{R \times 1}$  ( $R$  is the number of reaction rates, e.g.  $R = 8$  in the original [ASM1](#), [Henze et al. \(1987\)](#)).

The matrix  $\mathbf{M}$  combines the  $R$  rates to produce the  $N$  time derivatives of the states,  $\dot{\mathbf{x}}$ . Hence we have  $\mathbf{M} \in \mathbb{R}^{N \times R}$ . The additional term ( $\mathbf{z}$ ) in eq. (11) represents the *actuation* on the states of the system<sup>3</sup>.

Equation (12) (a.k.a. *measurement model* ([Ljung, 1999](#), ch. 4.3)) represents a mapping that generates measurement signals,  $\mathbf{y}$  (modelling those that could be produced by a sensor), based on the model states ( $\mathbf{x}$ ).

Until here we have omitted the dependence of eqs. (11)-(12) on parameters to keep the notation simple. All the model's components described till now can depend on parameters (free<sup>4</sup> and fundamental).

Many models for activated sludge and anaerobic digestion obey this structure, for example, all the [ASM](#) family ([Henze et al., 2000](#)), and several anaerobic digestions models ([Manchala et al., 2017](#)) such as [ADM1](#) ([Batstone et al., 2002](#)). As an example, all model components described above correspond to [ASM1](#) and can be found in [B.3](#), including tabs. 4 with all parameters and their description. This means that the analysis presented here can be applied to any model that follows the form in eqs. (11)-(12).

As the model evolves in time, eq. (11) provides the first time derivative of the signals. The second time derivative of all states is obtained by direct application of the chain rule:

$$\ddot{\mathbf{x}} = \mathbf{M} \dot{\mathbf{r}} + \dot{\mathbf{z}} = \mathbf{M} \mathbf{J}_r \dot{\mathbf{x}} + \dot{\mathbf{z}} \quad (13)$$

<sup>3</sup>The actuation might not be the inputs defined by a controller, a further *input model* ( $\mathbf{b}$ ) might be needed:  $\mathbf{z} := \mathbf{b}(\mathbf{u})$ , where  $\mathbf{u}$  are the controllable inputs and  $\mathbf{z}$  are the actuations

<sup>4</sup>parameters that must be estimated, e.g. experimentally

where  $\mathbf{J}_r$  is the Jacobian of the rates w.r.t. the states, i.e.

$$\mathbf{J}_r := \begin{bmatrix} \nabla_{\mathbf{x}}^\top r_1(\mathbf{x}) \\ \vdots \\ \nabla_{\mathbf{x}}^\top r_R(\mathbf{x}) \end{bmatrix} = \begin{bmatrix} \partial_{x_1} r_1 & \cdots & \partial_{x_N} r_1 \\ \vdots & \ddots & \vdots \\ \partial_{x_1} r_R & \cdots & \partial_{x_N} r_R \end{bmatrix} \quad (14)$$

The **ramps** of the  $i$ -th signal in these models is then given by

$$\text{ramps} := \{t : \mathbf{M}_{i,:} \mathbf{r} + z_i > 0 \wedge \mathbf{M}_{i,:} \mathbf{J}_r \dot{\mathbf{x}} + \dot{z}_i = 0\} \quad (15)$$

## 4.4 Ramp contingency

Here the typical and the physical minimum and maximum values are presented for all eight relevant states that can cause the  $S_{O_2}$  **ramp** feature.

For all the evaluations in this article, we used Python 3 (Van Rossum and Drake, 2009) and SymPy (Meurer et al., 2017) (any other computer algebra system could be used), complemented by a minimal amount of manual analysis that will be further automated in the future (Carbajal and Schneider, 2024).

## Acknowledgements

JPC is deeply grateful to Gustavo Buscaglia for the many insightful discussions that were had during the creation of this article.

## Funding sources

MYS was supported by the Swiss National Foundation (P500PT\_211132).

## Authors contributions

MYS: Conceptualisation, Formal Analysis, Methodology, Funding Acquisition, Software, Validation, Visualisation, Writing - Original Draft, Review & Editing ET: Validation, Writing - Original Draft, Review & Editing JPC: Conceptualisation, Formal Analysis, Methodology, Software, Validation, Visualisation, Writing - Original Draft, Review & Editing

## References

- N. Akashi, Y. Kuniyoshi, T. Jo, M. Nishida, R. Sakurai, Y. Wakao, and K. Nakajima. Embedding Bifurcations into Pneumatic Artificial Muscle. *Advanced Science*, 11(25):2304402, 2024. ISSN 2198-3844. doi: 10.1002/advs.202304402.
- I. A. Al-Ghusain, J. Huang, O. J. Hao, and B. S. Lim. Using pH as a real-time control parameter for wastewater treatment and sludge digestion processes. *Water Science and Technology*, 30(4):159–168, 1994. doi: 10.2166/wst.1994.0182.
- J. Alex, L. Benedetti, J. Copp, K. Gernaey, U. Jeppsson, I. Nopens, M.-N. Pons, J.-P. Steyer, and P. Vanrolleghem. *Benchmark Simulation Model no. 1 (BSM1)*, volume TEIE-7229. Lund University, 2008.
- J. Alferes, O. Grievson, C. Heffernan, D. Lumley, T. Massiri, A. Menniti, O. Samuelsson, K. Villez, and E. Zegers. Practical procedures for sensor quality assessment. In K. Villez, D. Aguado, J. Alferes, Q. Plana, M. V. Ruano, and O. Samuelsson, editors, *Metadata Collection and Organization in Wastewater Treatment and Wastewater Resource Recovery Systems*, pages 103–162. IWA Publishing, London, UK, June 2024. ISBN 978-1-78906-115-4. doi: 10.2166/9781789061154\_0103.
- S. Bathiany, H. Dijkstra, M. Crucifix, V. Dakos, V. Brovkin, M. S. Williamson, T. M. Lenton, and M. Scheffer. Beyond bifurcation: using complex models to understand and predict abrupt climate change. *Dynamics and Statistics of the Climate System*, 1(1):dzw004, Jan. 2016. ISSN 2059-6987. doi: 10.1093/climsys/dzw004.
- D. Batstone, J. Keller, I. Angelidaki, S. Kalyuzhnyi, S. Pavlostathis, A. Rozzi, W. Sanders, H. Siegrist, and V. Vavilin. The IWA Anaerobic Digestion Model No 1 (ADM1). *Water Science and Technology*, 45(10):65–73, May 2002. ISSN 0273-1223, 1996-9732. doi: 10.2166/wst.2002.0292.
- B. Benyahia, T. Sari, B. Cherki, and J. Harmand. Bifurcation and stability analysis of a two step model for monitoring anaerobic digestion processes. *Journal of Process Control*, 22(6):1008–1019, July 2012. ISSN 0959-1524. doi: 10.1016/j.jprocont.2012.04.012.

- A. Bornhöft, R. Hanke-Rauschenbach, and K. Sundmacher. Steady-state analysis of the Anaerobic Digestion Model No. 1 (ADM1). *Nonlinear Dynamics*, 73(1):535–549, July 2013. ISSN 1573-269X. doi: 10.1007/s11071-013-0807-x.
- K. Caluwaerts and J. P. Carbajal. Energy conserving constant shape optimization of tensegrity structures. *International Journal of Solids and Structures*, 58:117–127, 2015. ISSN 00207683. doi: 10.1016/j.ijsolstr.2014.12.023. ISBN: 0020-7683.
- J. P. Carbajal and M. Y. Schneider. SBR features, 2019. URL <https://sbrml.gitlab.io/sbrfeatures/>.
- J. P. Carbajal and M. Y. Schneider. dynamical systems analysis, 2024. URL <https://gitlab.com/sbrml/dsa-signal-features/>.
- J. P. Carbajal, D. A. Martin, and D. R. Chialvo. Learning by mistakes in memristor networks. *Physical Review E*, 105(5):054306, May 2022. doi: 10.1103/PhysRevE.105.054306. Publisher: American Physical Society.
- F. Cecconi, S. Reifsnnyder, R. Sobhani, A. Cisquella-Serra, M. Madou, and D. Rosso. Functional behaviour and microscopic analysis of ammonium sensors subject to fouling in activated sludge processes. *Environmental Science: Water Research & Technology*, 6(10):2723–2733, 2020. ISSN 2053-1400, 2053-1419. doi: 10.1039/D0EW00359J.
- P. B. Dhamole, R. R. Nair, S. F. D’Souza, and S. S. Lele. Denitrification of high strength nitrate waste. *Bioresource Technology*, 98(2):247–252, Jan. 2007. ISSN 0960-8524. doi: 10.1016/j.biortech.2006.01.019.
- D. Dionisi, A. A. Rasheed, and A. Majumder. A new method to calculate the periodic steady state of sequencing batch reactors for biological wastewater treatment: Model development and applications. *Journal of Environmental Chemical Engineering*, 4(3):3665–3680, Sept. 2016. ISSN 2213-3437. doi: 10.1016/j.jece.2016.07.032.
- T. Dockhorn, J. Felmeden, T. Hillenbrand, I. Kaufmann Alves, B. Kirschbaum, G. Langergraber, S. Lautenschlaeger, M. Maurer, S. Neuhausen, J. Sigglow, and H. Steinmetz. *Arbeitsblatt DWA-A 272 Grundsätze für die Planung und Implementierung Neuartiger Sanitärsysteme (NASS)*. DWA-Regelwerk. DWA, Hennef, Germany, first edition, June 2014. ISBN 978-3-944328-63-8.
- S. Eggimann, B. Truffer, U. Feldmann, and M. Maurer. Screening European market potentials for small modular wastewater treatment systems – an inroad to sustainability transitions in urban water management? *Land Use Policy*, 78:711–725, Nov. 2018. ISSN 0264-8377. doi: 10.1016/j.landusepol.2018.07.031.
- F. Grogard and O. Bernard. Stability analysis of a wastewater treatment plant with saturated control. *Water Science and Technology*, 53(1):149–157, Jan. 2006. ISSN 0273-1223. doi: 10.2166/wst.2006.017.
- W. Gujer and M. Henze. Activated Sludge Modelling and Simulation. *Water Science and Technology*, 23:1011–1023, Feb. 1991. doi: 10.2166/wst.1991.0553.
- H. Haimi, M. Mulas, F. Corona, and R. Vahala. Data-derived soft-sensors for biological wastewater treatment plants: An overview. *Environmental Modelling & Software*, 47:88–107, Sept. 2013. doi: 10.1016/j.envsoft.2013.05.009.
- G. Haller. *Transport barriers and coherent structures in flow data: advective, diffusive, stochastic and active methods*. Cambridge university press, Cambridge, 2023. ISBN 978-1-00-922517-5.
- H. Hauduc, L. Rieger, I. Takács, A. Héduit, P. A. Vanrolleghem, and S. Gillot. A systematic approach for model verification: application on seven published activated sludge models. *Water Science and Technology*, 61(4):825–839, Feb. 2010. ISSN 0273-1223. doi: 10.2166/wst.2010.898. eprint: <https://iwaponline.com/wst/article-pdf/61/4/825/1044907/825.pdf>.
- M. Henze, C. P. L. Grady, W. Gujer, G. V. R. Marais, and T. Matsuo. A general model for single-sludge wastewater treatment systems. *Water Research*, 21(5):505–515, May 1987. ISSN 0043-1354. doi: 10.1016/0043-1354(87)90058-3.
- M. Henze, W. Gujer, T. Mino, and M. C. M. van Loosdrecht. *Activated sludge models ASM1, ASM2, ASM2d and ASM3*. IWA publishing. IWA, London, UK, 2000. ISBN 978-1-900222-24-2.
- S. W. How, J. H. Sin, S. Y. Y. Wong, P. B. Lim, A. Mohd Aris, G. C. Ngoh, T. Shoji, T. P. Curtis, and A. S. M. Chua. Characterization of slowly-biodegradable organic compounds and hydrolysis kinetics in tropical wastewater for biological nitrogen removal. *Water Science and Technology*, 81(1):71–80, Feb. 2020. ISSN 0273-1223. doi: 10.2166/wst.2020.077.
- H. L. Ivan and V. Zaccaria. Exploring the effects of faults on the performance of a biological wastewater treatment process. *Water Science and Technology*, 90(2):474–489, June 2024. ISSN 0273-1223. doi: 10.2166/wst.2024.213.
- T. A. Larsen, S. Hoffmann, C. Lüthi, B. Truffer, and M. Maurer. Emerging solutions to the water challenges of an urbanizing world. *Science*, 352(6288):928–933, May 2016. doi: 10.1126/science.aad8641.
- B. Li, S. Mao, T. Tian, H. Bi, Y. Tian, X. Ma, and Y. Qiu. Design and application of soft sensors in rural sewage treatment facilities. *AQUA - Water Infrastructure, Ecosystems and Society*, 72(11):2001–2016, Nov. 2023. ISSN 2709-8028. doi: 10.2166/aqua.2023.062.

- L. Ljung. *System identification: theory for the user*. Prentice Hall PTR, 2nd editio edition, 1999. ISBN 978-0-13-656695-3.
- K. S. Lowe, M. B. Tucholke, J. M. Tomaras, K. Conn, C. Hoppe, J. E. Drewes, J. E. McCray, and J. Munakata-Marr. Influent Constituent Characteristics of the Modern Waste Stream from Single Sources: Final Report, Sept. 2009. URL [http://web.archive.org/web/20190216024758/http://www.decentralizedwater.org/research\\_project\\_04-DEC-1.asp](http://web.archive.org/web/20190216024758/http://www.decentralizedwater.org/research_project_04-DEC-1.asp).
- K. R. Manchala, Y. Sun, D. Zhang, and Z.-W. Wang. Anaerobic Digestion Modelling. In *Advances in Bioenergy*, volume 2, pages 69–141. Elsevier, 2017. ISBN 978-0-12-812286-0. doi: 10.1016/bs.aibe.2017.01.001.
- A. Meurer, C. P. Smith, M. Paprocki, O. Čertík, S. B. Kirpichev, M. Rocklin, A. Kumar, S. Ivanov, J. K. Moore, S. Singh, T. Rathnayake, S. Vig, B. E. Granger, R. P. Muller, F. Bonazzi, H. Gupta, S. Vats, F. Johansson, F. Pedregosa, M. J. Curry, A. R. Terrel, v. Roučka, A. Saboo, I. Fernando, S. Kulal, R. Cimrman, and A. Scopatz. Sympy: symbolic computing in python. *PeerJ Computer Science*, 3:e103, Jan. 2017. ISSN 2376-5992. doi: 10.7717/peerj-cs.103.
- M. I. Nelson and H. S. Sidhu. Analysis of the activated sludge model (number 1). *Applied Mathematics Letters*, 22(5):629–635, May 2009. ISSN 0893-9659. doi: 10.1016/j.aml.2008.05.003.
- O. B. L. Neto, M. Mulas, and F. Corona. About the classical and structural controllability and observability of a common class of activated sludge plants. *Journal of Process Control*, 111:8–26, Mar. 2022. ISSN 0959-1524. doi: 10.1016/j.jprocont.2021.12.013.
- K. Ohmura, C. M. Thürlimann, M. Kipf, J. P. Carbajal, and K. Villez. Characterizing long-term wear and tear of ion-selective pH sensors. *Water Science and Technology*, 80(3):541–550, Aug. 2019. ISSN 0273-1223, 1996-9732. doi: 10.2166/wst.2019.301.
- G. Olsson and J. F. Andrews. The dissolved oxygen profile—A valuable tool for control of the activated sludge process. *Water Research*, 12(11):985–1004, Jan. 1978. ISSN 0043-1354. doi: 10.1016/0043-1354(78)90082-9.
- J. Pearl and D. Mackenzie. *The Book of Why: The New Science of Cause and Effect*. Penguin Books Limited, 2018. ISBN 978-0-241-24264-3.
- K. Rabaey, T. Vandekerckhove, A. V. de Walle, and D. L. Sedlak. The third route: Using extreme decentralization to create resilient urban water systems. *Water Research*, 185:116276, Oct. 2020. ISSN 0043-1354. doi: 10.1016/j.watres.2020.116276.
- P. Racho and A. Pongampornnara. Enhanced biogas production from modified tapioca starch wastewater. *Energy Reports*, 6: 744–750, 2020. ISSN 2352-4847. doi: <https://doi.org/10.1016/j.egy.2019.09.058>.
- E. Reynaert, P. Steiner, Q. Yu, L. D. Olif, N. Joller, M. Y. Schneider, and E. Morgenroth. Predicting Microbial Water Quality in On-Site Water Reuse Systems with Online Sensors. *Water Research*, page 120075, May 2023. ISSN 0043-1354. doi: 10.1016/j.watres.2023.120075.
- F. E. Rosas, B. C. Geiger, A. I. Luppi, A. K. Seth, D. Polani, M. Gastpar, and P. A. M. Mediano. Software in the natural world: A computational approach to hierarchical emergence, June 2024. URL <http://arxiv.org/abs/2402.09090>. arXiv:2402.09090 [nlin].
- E. Sampaio, M. Mulas, O. Neto, and F. Corona. Structural analysis of an activated sludge process with greenhouse gas emissions, Nov. 2022.
- O. Samuelsson, A. Björk, J. Zambrano, and B. Carlsson. Fault signatures and bias progression in dissolved oxygen sensors. *Water Science and Technology*, 78(5):1034–1044, Oct. 2018. ISSN 0273-1223, 1996-9732. doi: 10.2166/wst.2018.350.
- M. Y. Schneider, J. P. Carbajal, V. Furrer, B. Sterkele, M. Maurer, and K. Villez. Beyond signal quality: The value of unmaintained pH, dissolved oxygen, and oxidation-reduction potential sensors for remote performance monitoring of on-site sequencing batch reactors. *Water Research*, 161:639–651, Sept. 2019. ISSN 00431354. doi: 10.1016/j.watres.2019.06.007.
- M. Y. Schneider, V. Furrer, E. Sprenger, J. P. Carbajal, K. Villez, and M. Maurer. Benchmarking Soft Sensors for Remote Monitoring of On-Site Wastewater Treatment Plants. *Environmental Science & Technology*, 54(17):10840–10849, Sept. 2020. ISSN 0013-936X, 1520-5851. doi: 10.1021/acs.est.9b07760.
- M. Y. Schneider, W. Quaghebeur, S. Borzooei, A. Froemelt, F. Li, R. Saagi, M. J. Wade, J.-J. Zhu, and E. Torfs. Hybrid modelling of water resource recovery facilities: status and opportunities. *Water Science and Technology*, 85(9):2503–2524, Apr. 2022. ISSN 0273-1223. doi: 10.2166/wst.2022.115.
- S. Shen, G. C. Premier, A. Guwy, and R. Dinsdale. Bifurcation and stability analysis of an anaerobic digestion model. *Nonlinear Dynamics*, 48(4):391–408, June 2007. ISSN 1573-269X. doi: 10.1007/s11071-006-9093-1.
- H.-Y. Shyu, C. J. Castro, R. A. Bair, Q. Lu, and D. H. Yeh. Development of a Soft Sensor Using Machine Learning Algorithms for Predicting the Water Quality of an Onsite Wastewater Treatment System. *ACS Environmental Au*, June 2023. doi: 10.1021/acsenvironau.2c00072. Publisher: American Chemical Society.

- S. Strogatz. *Nonlinear dynamics and chaos: with applications to physics, biology, chemistry, and engineering*. CRC Press, Boca Raton, third edition edition, 2024. ISBN 978-1-03-266521-4. OCLC: 1406021569.
- C. M. Thürlimann, K. M. Udert, E. Morgenroth, and K. Villez. Stabilizing control of a urine nitrification process in the presence of sensor drift. *Water Research*, 165:114958, Nov. 2019. ISSN 00431354. doi: 10.1016/j.watres.2019.114958.
- M. C. M. van Loosdrecht and D. Brdjanovic. Anticipating the next century of wastewater treatment. *Science*, 344(6191): 1452–1453, June 2014. ISSN 0036-8075, 1095-9203. doi: 10.1126/science.1255183. Publisher: American Association for the Advancement of Science Section: Perspective.
- G. Van Rossum and F. L. Drake. *Python 3 Reference Manual*. CreateSpace, Scotts Valley, CA, 2009. ISBN 1441412697.
- P. A. Vanrolleghem. *On-line Modelling of Activated Sludge Processes: Development of an Adaptive Sensor*. Ph.D. thesis, Ghent Univeristy, Gent, Belgium, Feb. 1994. URL <https://modeleau.fsg.ulaval.ca/index.php?id=377>.
- E. Volcke, M. Sbarciog, E. Noldus, B. De Baets, and M. Loccufier. Steady state multiplicity of two-step biological conversion systems with general kinetics. *Mathematical Biosciences*, 228(2):160–170, Dec. 2010. ISSN 00255564. doi: 10.1016/j.mbs.2010.09.004.
- M. J. Wade and G. S. K. Wolkowicz. Bifurcation Analysis of an Impulsive System Describing Partial Nitritation and Anammox in a Hybrid Reactor. *Environmental Science & Technology*, 55(3):2099–2109, Feb. 2021. ISSN 0013-936X. doi: 10.1021/acs.est.0c06275. Publisher: American Chemical Society.
- S. Zhong, K. Zhang, M. Bagheri, J. G. Burken, A. Gu, B. Li, X. Ma, B. L. Marrone, Z. J. Ren, J. Schrier, W. Shi, H. Tan, T. Wang, X. Wang, B. M. Wong, X. Xiao, X. Yu, J.-J. Zhu, and H. Zhang. Machine Learning: New Ideas and Tools in Environmental Science and Engineering. *Environmental Science & Technology*, 55(19):12741–12754, Oct. 2021. ISSN 0013-936X. doi: 10.1021/acs.est.1c01339. Publisher: American Chemical Society.

## A Supplementary information

### A.1 Time derivatives

Here we detail the calculation for the time derivative of a model with the following structure

$$\dot{\mathbf{x}} = \mathbf{M}\mathbf{r}(\mathbf{x}) \quad (16)$$

to which we introduce a new term in the derivatives

$$\dot{\mathbf{x}} = \mathbf{M}\mathbf{r}(\mathbf{x}) + \mathbf{z}(\mathbf{x}, t) \quad (17)$$

By direct derivation, the second time derivative reads (we do not show the explicit dependence anymore):

$$\ddot{\mathbf{x}} = \mathbf{M}\dot{\mathbf{r}} + \dot{\mathbf{z}} \quad (18)$$

$$\dot{\mathbf{r}} = \partial_{\mathbf{x}}\mathbf{r} \dot{\mathbf{x}} \quad (19)$$

$$\dot{\mathbf{z}} = \partial_{\mathbf{x}}\mathbf{z} \dot{\mathbf{x}} + \partial_t\mathbf{z} \quad (20)$$

replacing

$$\ddot{\mathbf{x}} = \mathbf{M}\partial_{\mathbf{x}}\mathbf{r} \dot{\mathbf{x}} + \partial_{\mathbf{x}}\mathbf{z} \dot{\mathbf{x}} + \partial_t\mathbf{z} \quad (21)$$

Another approach is to think that the introduction of the derivatives modifies the structure of the system in (16):

$$\dot{\mathbf{x}} = \mathbf{M}^*\mathbf{r}^*(\mathbf{x}) \quad (22)$$

with the new elements being concatenations of the old

$$\mathbf{M}^* = \begin{bmatrix} \mathbf{M} & \mathbb{I}_{\dim \mathbf{z}} \end{bmatrix} \quad (23)$$

$$\mathbf{r}^*(\mathbf{x}) = \begin{bmatrix} \mathbf{r}(\mathbf{x}) \\ \mathbf{z}(\mathbf{x}, t) \end{bmatrix} \quad (24)$$

where  $\mathbb{I}_{\dim \mathbf{z}}$  is the identity matrix of the size of  $\mathbf{z}$ . Expanding:

$$\mathbf{M}^*\mathbf{r}^* = \begin{bmatrix} \mathbf{M} & \mathbb{I}_{\dim \mathbf{z}} \end{bmatrix} \begin{bmatrix} \mathbf{r} \\ \mathbf{z} \end{bmatrix} = \mathbf{M}\mathbf{r} + \mathbf{z} \quad (25)$$

which shows the equivalence to eq. (17). In this case the second derivative is,

$$\ddot{\mathbf{x}} = \mathbf{M}^*\dot{\mathbf{r}}^* = \mathbf{M}^*(\partial_{\mathbf{x}}\mathbf{r}^* \dot{\mathbf{x}} + \partial_t\mathbf{r}^*) \quad (26)$$

which gives a simple general formula applicable also in the absence of actuation.

To verify equality with the previous derivation we expand the terms. Computing the Jacobian

$$\partial_{\mathbf{x}}\mathbf{r}^* = \partial_{\mathbf{x}} \begin{bmatrix} \mathbf{r} \\ \mathbf{z} \end{bmatrix} = \begin{bmatrix} \partial_{\mathbf{x}}\mathbf{r} \\ \partial_{\mathbf{x}}\mathbf{z} \end{bmatrix} \quad (27)$$

then

$$\partial_{\mathbf{x}}\mathbf{r}^* \dot{\mathbf{x}} = \begin{bmatrix} \partial_{\mathbf{x}}\mathbf{r} \\ \partial_{\mathbf{x}}\mathbf{z} \end{bmatrix} \dot{\mathbf{x}} = \begin{bmatrix} \partial_{\mathbf{x}}\mathbf{r} \dot{\mathbf{x}} \\ \partial_{\mathbf{x}}\mathbf{z} \dot{\mathbf{x}} \end{bmatrix} \quad (28)$$

and

$$\mathbf{M}^*\partial_{\mathbf{x}}\mathbf{r}^* \dot{\mathbf{x}} = \begin{bmatrix} \mathbf{M} & \mathbb{I}_{\dim \mathbf{z}} \end{bmatrix} \begin{bmatrix} \partial_{\mathbf{x}}\mathbf{r} \dot{\mathbf{x}} \\ \partial_{\mathbf{x}}\mathbf{z} \dot{\mathbf{x}} \end{bmatrix} = \mathbf{M}\partial_{\mathbf{x}}\mathbf{r} \dot{\mathbf{x}} + \partial_{\mathbf{x}}\mathbf{z} \dot{\mathbf{x}} \quad (29)$$

The temporal term is

$$\mathbf{M}^*\partial_t\mathbf{r}^* = \begin{bmatrix} \mathbf{M} & \mathbb{I}_{\dim \mathbf{z}} \end{bmatrix} \begin{bmatrix} \partial_t\mathbf{r} \\ \partial_t\mathbf{z} \end{bmatrix} = \mathbf{M} \overbrace{\partial_t\mathbf{r}}^{\mathbf{0}} + \partial_t\mathbf{z} \quad (30)$$

Putting all together

$$\ddot{\mathbf{x}} = \mathbf{M}\partial_{\mathbf{x}}\mathbf{r} \dot{\mathbf{x}} + \partial_{\mathbf{x}}\mathbf{z} \dot{\mathbf{x}} + \partial_t\mathbf{z} \quad (31)$$

which is the same as eq. (21).

### A.1.1 Single state actuation

If we assume that the actuation does not depend directly on time, and only depends in a single state, the actuation vector has the form:

$$\mathbf{z}(\mathbf{x}, t) = \mathbf{1}_{x_i} z(x_i) \quad (32)$$

where  $\mathbf{1}_{x_i}$  is a column vector filled with zeros, except in the location of element  $x_i$ . That is,  $\mathbf{z}$  affects only the state  $x_i$  and it depends only on that state.

We have that

$$\partial_t \mathbf{z} = \mathbf{0} \quad (33)$$

$$\partial_{\mathbf{x}} \mathbf{z} \dot{\mathbf{x}} = \partial_{\mathbf{x}} \mathbf{1}_{x_i} z(x_i) \dot{\mathbf{x}} = \partial_{x_i} z \mathbf{1}_{x_i} \dot{x}_i = \partial_{x_i} z \dot{x}_i \mathbf{1}_{x_i} \quad (34)$$

where  $\mathbf{1}_{x_i x_i}$  is a matrix with a 1 in the  $(x_i, x_i)$  element, and zero otherwise. By replacing into eq. (31) we obtain,

$$\ddot{\mathbf{x}} = M \partial_{\mathbf{x}} \mathbf{r} \dot{\mathbf{x}} + \partial_{x_i} z \dot{x}_i \mathbf{1}_{x_i} \quad (35)$$

and the  $x_i$  component is

$$\ddot{x}_i = M_{x_i} \partial_{\mathbf{x}} \mathbf{r} \dot{\mathbf{x}} + \partial_{x_i} z \dot{x}_i \quad (36)$$

These are the formulas used in the software (Carbajal and Schneider, 2024) accompanying this publication.

## B Ramp points curve

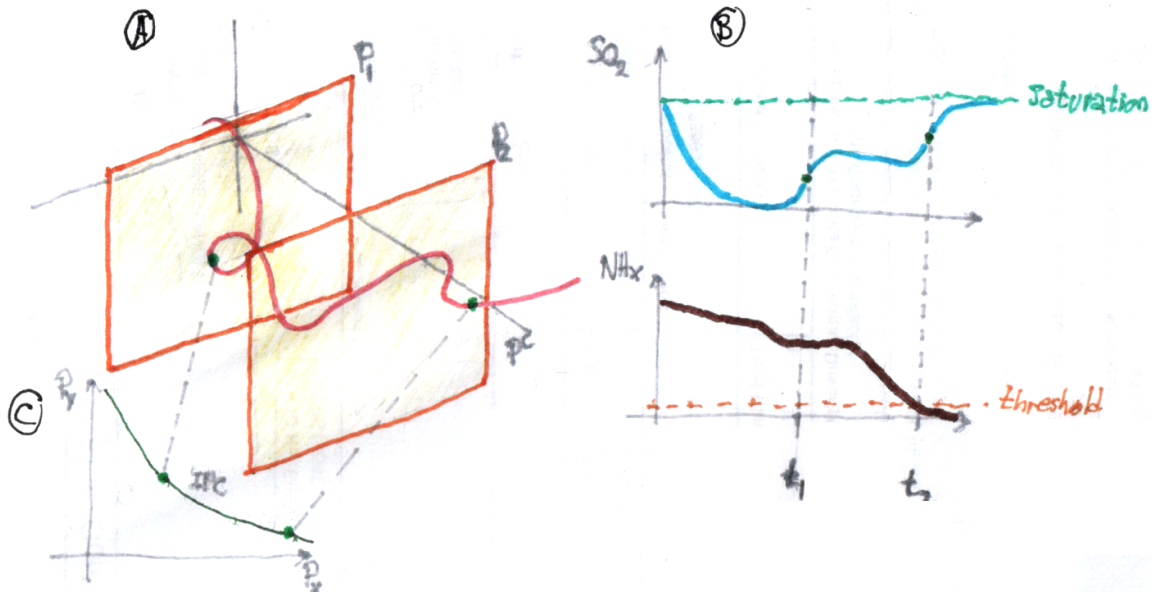


Figure 7: Construction and interpretation of **ramp** points curve. A: a trajectory of a dynamical system in  $\mathbb{R}^N$ . In the drawing, the space is decomposed in two sub-spaces of dimension 2 (the planes are labelled with  $P$  in the diagram), and  $N - 2$  (the perpendicular direction to the planes, the orthogonal complement  $P^\perp$  of  $P$ ). By fixing the values of all components of a vector in  $P^\perp$  a plane is defined as shown. The trajectory crosses these planes as it evolves. B: Components of the trajectory can be plotted as a function of time, as an example the states  $S_{O_2}$  and  $NH_x$  from [ASM1](#) are shown. The points in which a ramp is realised are marked here and in the trajectory. The time of the ramps have their corresponding planes in panel A,  $t_1$  with  $P_1$ , etc. C: By merging all the planes and the points corresponding to a **ramp** in them, we obtain the locus of all ramps. These loci might look like curves in the obtained plot. The curve collects points from different planes (different values of the states in  $P^\perp$ )

The locus of all ramps defines a hyper-surface of dimension  $\mathbb{R}^{N-1}$ . This surface cannot be visualized easily. Therefore we choose a sub-space of dimension 2 that we call  $P$  (for plane) and we collect points fulfilling the ramp conditions in it.

In  $P$  we have two states of our choice, e.g.  $S_{O_2}$  and  $X_a$ , and all other states are in the orthogonal complement of  $P$ , called  $P^\perp$ . In fig. 7 we depict  $P^\perp$  as a single direction, but the reader should understand that in fact, this sub-space is of dimension  $N - 2$ .

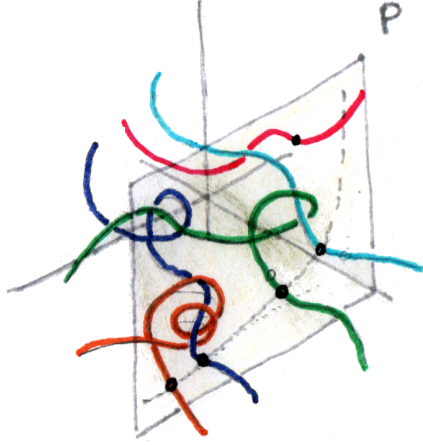


Figure 8: Multiple trajectories crossing the plane  $P$ , for fixed values of  $P^\perp$ . Some trajectories intersect the plane with a ramp in the time signal of the selected component, e.g.  $S_{O_2}$ , while others do not (pink trajectory). Only those with a ramp contribute to the ramp locus (dashed lines on  $P$ ).

To put a ramp point in  $P$ , we must first define a value for all states in  $P^\perp$ . These are the planes shown in panel A of fig. 7. For any value we choose for these other states, and for any value of the states in  $P$ , we can always find a trajectory of the dynamical system that goes through the point in the full space. Hence, the reader should imagine each of these planes crossed by many trajectories as the ones shown here, each one intersecting the plane at a unique point. We then filter the intersection points by selecting those that fulfil the ramp condition. Then we repeat this process for different values of the states in  $P^\perp$  (different planes in the figure). We collect all these points in a single plane. These are the curves shown in fig. 4 in the body of the article.

The points shown in fig. 5 are obtained in a similar fashion. However, for these points, we do not fix any state. All states (including  $S_{NH_x}$ ) are free, and to sample the hyper-surface defined by the ramp conditions (9) and (10), we solve an optimisation problem, which can be stated as follows: generate distinct points in a level set defined by a function  $\phi : \mathbb{R}^n \rightarrow \mathbb{R}$  (in our case  $n = 8$ ):

$$\mathcal{L}_c := \{x \in \mathbb{R}^n : \phi(x) = c\} \quad (37)$$

To warrant good behaviour of the set, we assume that the function has the following properties:

1. is continuous: implies closedness of the sets  $\{x \in \mathbb{R}^n : \phi(x) \leq c\}$  (sublevel set)
2.  $\nabla\phi(x) \neq 0 \quad \forall x \in \mathcal{L}_c$  (non-degenerate level set, level sets don't intersect)
3. is coercive:  $\lim_{\|x\| \rightarrow \infty} \phi(x) = \infty$  (compact sublevel sets). That is:  $\phi$  is coercive  $\iff \forall c \in \mathbb{R}, \{x \in \mathbb{R}^n : \phi(x) \leq c\}$  is compact.

We can set the problem of sampling the ramp hyper-surface as a constrained optimization:

$$x = \arg \min_{x \in S \subset \mathbb{R}^n} f(x, \theta) \quad (38)$$

$$\phi(x) = 0 \quad \text{eq. (9)} \quad (39)$$

$$\psi(x) > 0 \quad \text{eq. (10)} \quad (40)$$

where  $S$  is chosen such that  $\mathcal{L}_c \cap S \neq \emptyset$  (e.g. a hyperbox), and the cost function  $f(x) : \mathbb{R}^n \rightarrow \mathbb{R}$  is arbitrary. The quality of the optimization results for our sampling can be verified by looking at the distributions shown in fig. 9. There the values of  $\phi(x)$  are shown (second time derivative, which should be zero), together with the values of  $\psi(x)$  (first time derivative, must be positive).

The cost function is exploited to achieve other objectives, like the spread of the points over the surface. For example:

$$f(x, \{x_i\}_{1 \leq i \leq I}, r_{\min}) = - \sum_{i=1}^I H(r_{\min} - \|x - x_i\|) \|x - x_i\|^2 \quad (41)$$

where  $\{x_i\}_{1 \leq i \leq I}$  is a set of points in  $\mathcal{L}_c$  (e.g. the set of previous solutions to the problem).  $H(r)$  is the step function, with value 1 when  $r > 0$ .

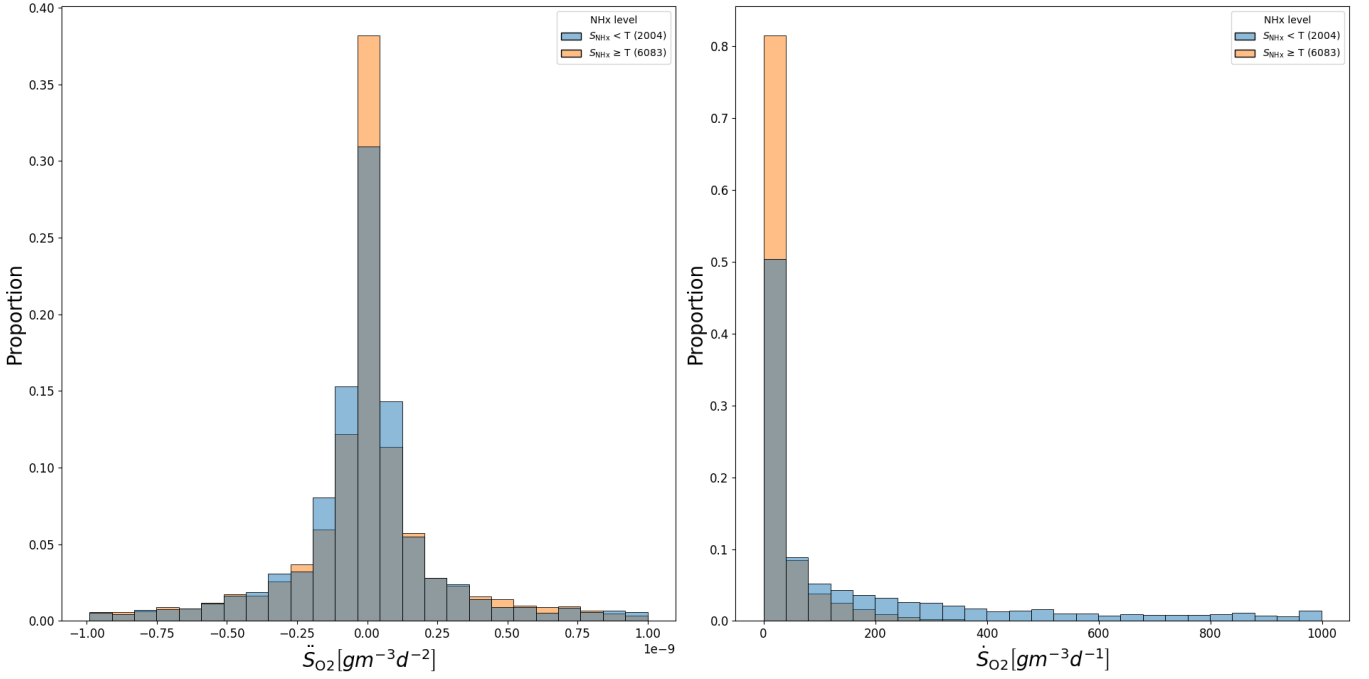


Figure 9: Values of the dissolved oxygen time derivatives of the selected samples from fig. 5

Numerical solutions using Sequential Quadratic Programming (SQP) showed an accumulation of solutions on the boundary of the intersection  $\mathcal{L}_c \cap S$ , likely due to the Karush–Kuhn–Tucker conditions. Other constrained optimizers are to be tested, but as a workaround, the cost function can be extended to

$$\tilde{f}(x, \{x_i\}_{1 \leq i \leq I}, \partial S) = f(x, \{x_i\}_{1 \leq i \leq I}) + \text{spike}(x, \partial S) \quad (42)$$

where spike is a function that increases rapidly as  $x$  approaches the boundary ( $\partial S$ ) of  $S$ . This workaround and a very tight hyperbox provided the results reported.

## B.1 Interpretability of the inflection point curve

Figure 10 is the result from an interactive plot where points in the  $(X_h, S_{O_2})$  plane can be selected and the time-series are reproduced from these points. The point on the blue line in the top figures are **ramps**, the points away from the curve or instances where no ramp occurs. From these points then the dissolved oxygen signals are reconstructed. This illustrates the simulation time that we save by computing the inflection point curve directly. Hence, we evaluated **ramps** for 100,000 initial conditions in a few minutes on a normal laptop, which covers a large region of the state-space.

## B.2 Symbols name

## B.3 ASM1 model

$$\mathbf{x} = \begin{bmatrix} S_{nb} \\ S_b \\ X_{nb,in} \\ X_{cb} \\ X_h \\ X_a \\ X_{nb,e} \\ S_{O_2} \\ S_{NO_x} \\ S_{NH_x} \\ S_{bN} \\ X_{cbN} \\ S_{alk} \\ S_{N_2} \end{bmatrix} \quad (43)$$

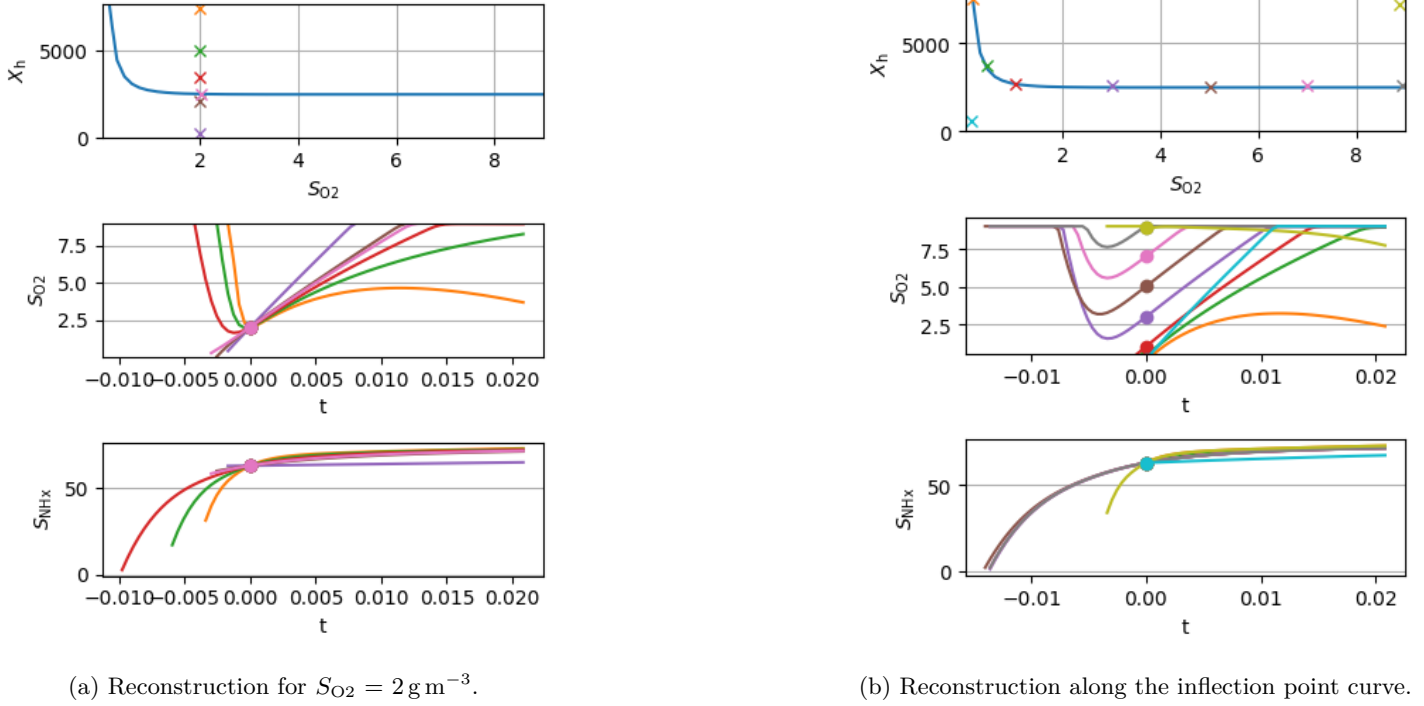


Figure 10: Reconstruction of the  $S_{O_2}$  and  $S_{NH_x}$  curve from selected points, marked with an x, in the  $S_{O_2}$ ,  $X_h$  plane. In a) only one value is on the inflection point curve, hence has a **ramp**, in b) all but the two in the bottom left and upper right corner are combinations of states with ammonium above the threshold leading to **ramps**.

This work	Other name	Description
$S_b$	$S_B$	Soluble biodegradable organics (SS)
$S_{nb}$	$S_U$	Soluble nondegradable organics (SI)
$S_{O_2}$	$S_{O_2}$	Dissolved oxygen (SO)
$X_{cb}$	$X_{CB}$	Particulate and colloidal biodegradable organics (XS)
$X_{nb,in}$	$X_{UInf}$	Particulate nonbiodegradable organics from the influent (XI)
$X_{nb,e}$	$X_{UE}$	Particulate nonbiodegradable endogenous products (XP)
$S_{NH_x}$	$S_{NH_x}$	Ammonia ( $NH_4 + NH_3$ ) (SNH)
$S_{NO_x}$	$S_{NO_x}$	Nitrate and nitrite ( $NO_3 + NO_2$ ) (considered to be $NO_3$ only for stoichiometry, SNO)
$X_{cbN}$	$X_{CBN}$	Particulate and colloidal biodegradable organic N (XND)
$S_{bN}$	$S_{BN}$	Soluble biodegradable organic N (SND)
$X_h$	$X_{OHO}$	Ordinary heterotrophic organisms (XBH)
$X_a$	$X_{ANO}$	Autotrophic nitrifying organisms ( $NH_4^+$ to $NO_3^-$ , XBA)
$S_{alk}$	$S_{Alk}$	Alkalinity ( $HCO_3^-$ , SALK)
$S_{N_2}$	$S_{N_2}$	Dissolved nitrogen (gas, $N_2$ ), not in classic ASM1

Table 2: Naming of states in this work in relation to commonly used names, e.g. (Henze et al., 2000), which is provided in the bracket in the description. The "other name" column is based on (Hauduc et al., 2010).

This work	Other name	Description
$g_{hO_2}$	$g_{hO_2}$	Aerobic growth of heterotrophs
$g_{hAn}$	$g_{hAn}$	Anoxic growth of heterotrophs
$g_{aO_2}$	$g_{aO_2}$	Aerobic growth of autotrophs
$d_h$	$d_h$	Decay of heterotrophs
$d_a$	$d_a$	Decay of autotrophs
$a_N$	$am_N$	Ammonification of soluble organic nitrogen
$h_o$	$ho$	Hydrolysis of entrapped organics
$h_{oN}$	$ho_N$	Hydrolysis of entrapped organic nitrogen

Table 3: Naming of process rates and their description. The "other name" column is following (Hauduc et al., 2010).

$$\mathbf{M} = \begin{bmatrix}
0 & 0 & 0 & 0 & 0 & 0 & 0 & 0 \\
m_{S_b, g_{hO_2}} & m_{S_b, g_{hAn}} & 0 & 0 & 0 & 0 & 1 & 0 \\
0 & 0 & 0 & 0 & 0 & 0 & 0 & 0 \\
0 & 0 & 0 & m_{X_{cb}, d_h} & m_{X_{cb}, d_a} & 0 & -1 & 0 \\
1 & 1 & 0 & -1 & 0 & 0 & 0 & 0 \\
0 & 0 & 1 & 0 & -1 & 0 & 0 & 0 \\
0 & 0 & 0 & m_{X_{nb,e}, d_h} & m_{X_{nb,e}, d_a} & 0 & 0 & 0 \\
m_{S_{O_2}, g_{hO_2}} & 0 & m_{S_{O_2}, g_{aO_2}} & 0 & 0 & 0 & 0 & 0 \\
0 & m_{S_{NOx}, g_{hAn}} & m_{S_{NOx}, g_{aO_2}} & 0 & 0 & 0 & 0 & 0 \\
m_{S_{NHx}, g_{hO_2}} & m_{S_{NHx}, g_{hAn}} & m_{S_{NHx}, g_{aO_2}} & 0 & 0 & 1 & 0 & 0 \\
0 & 0 & 0 & 0 & 0 & -1 & 0 & 1 \\
0 & 0 & 0 & m_{X_{cbN}, d_h} & m_{X_{cbN}, d_a} & 0 & 0 & -1 \\
m_{S_{alk}, g_{hO_2}} & m_{S_{alk}, g_{hAn}} & m_{S_{alk}, g_{aO_2}} & 0 & 0 & m_{S_{alk}, a_N} & 0 & 0 \\
0 & m_{S_{N_2}, g_{hAn}} & 0 & 0 & 0 & 0 & 0 & 0
\end{bmatrix} \quad (44)$$

$$m_{S_b, g_{hO_2}} := -\frac{1}{\gamma_h} \quad (45)$$

$$m_{S_b, g_{hAn}} := -\frac{1}{\gamma_h} \quad (46)$$

$$m_{X_{cb}, d_h} := 1 - \zeta_{Xnb,l} \quad (47)$$

$$m_{X_{cb}, d_a} := 1 - \zeta_{Xnb,l} \quad (48)$$

$$m_{X_{nb,e}, d_h} := \zeta_{Xnb,l} \quad (49)$$

$$m_{X_{nb,e}, d_a} := \zeta_{Xnb,l} \quad (50)$$

$$m_{S_{O_2}, g_{hO_2}} := \frac{\gamma_h - 1}{\gamma_h} \quad (51)$$

$$m_{S_{O_2}, g_{aO_2}} := \frac{\gamma_a + \iota_{COD,NO_3}}{\gamma_a} \quad (52)$$

$$m_{S_{NOx}, g_{hAn}} := \frac{\gamma_h - 1}{\gamma_h \iota_{NO_3, N_2}} \quad (53)$$

$$m_{S_{NOx}, g_{aO_2}} := \frac{1}{\gamma_a} \quad (54)$$

$$m_{S_{NHx}, g_{hO_2}} := -\iota_{NXb} \quad (55)$$

$$m_{S_{NHx}, g_{hAn}} := -\iota_{NXb} \quad (56)$$

$$m_{S_{NHx}, g_{aO_2}} := -\iota_{NXb} - \frac{1}{\gamma_a} \quad (57)$$

$$m_{X_{cbN}, d_h} := \iota_{NXb} - \iota_{NXnb} \zeta_{Xnb,l} \quad (58)$$

$$m_{X_{cbN}, d_a} := \iota_{NXb} - \iota_{NXnb} \zeta_{Xnb,l} \quad (59)$$

$$m_{S_{alk}, g_{hO_2}} := -\iota_{NXb} \iota_{cSNHx} \quad (60)$$

$$m_{S_{alk}, g_{hAn}} := -\iota_{NXb} \iota_{cSNHx} + \frac{\iota_{cSNOx} (\gamma_h - 1)}{\gamma_h \iota_{NO_3, N_2}} \quad (61)$$

$$m_{S_{alk}, g_{aO_2}} := \iota_{cSNHx} \left( -\iota_{NXb} - \frac{1}{\gamma_a} \right) + \frac{\iota_{cSNOx}}{\gamma_a} \quad (62)$$

$$m_{S_{alk}, a_N} := \iota_{cSNHx} \quad (63)$$

$$m_{S_{N_2}, g_{hAn}} := \frac{1 - \gamma_h}{\gamma_h \iota_{NO_3, N_2}} \quad (64)$$

$$\quad (65)$$

$$\mathbf{r} = \begin{bmatrix}
g_{hO_2}(S_{NHx}, S_{O_2}, S_b, X_h) \\
g_{hAn}(S_{NHx}, S_{NOx}, S_{O_2}, S_b, X_h) \\
g_{aO_2}(S_{NHx}, S_{O_2}, X_a) \\
d_h(X_h) \\
d_a(X_a) \\
a_N(S_b, X_h) \\
h_o(S_{NOx}, S_{O_2}, X_{cb}, X_h) \\
h_{oN}(S_{NOx}, S_{O_2}, X_{cbN}, X_{cb}, X_h)
\end{bmatrix} \quad (66)$$

$$g_{\text{hO}_2}(S_{\text{NH}_x}, S_{\text{O}_2}, S_b, X_h) := S_{\text{NH}_x} S_b X_h \mu_{\text{max},h} \frac{S_{\text{O}_2}}{(S_{\text{NH}_x} + \kappa_{\text{NH}_x,h})(S_{\text{O}_2} + \kappa_{\text{O}_2,h})(S_b + \kappa_b)} \quad (67)$$

$$g_{\text{hAn}}(S_{\text{NH}_x}, S_{\text{NO}_x}, S_{\text{O}_2}, S_b, X_h) := S_{\text{NH}_x} S_b X_h \mu_{\text{max},h} \frac{S_{\text{NO}_x} \eta_{\text{an},h} \kappa_{\text{O}_2,h}}{(S_{\text{NH}_x} + \kappa_{\text{NH}_x,h})(S_{\text{O}_2} + \kappa_{\text{O}_2,h})(S_b + \kappa_b)(S_{\text{NO}_x} + \kappa_{\text{NO}_x,h})} \quad (68)$$

$$g_{\text{aO}_2}(S_{\text{NH}_x}, S_{\text{O}_2}, X_a) := \frac{S_{\text{NH}_x} S_{\text{O}_2} X_a \mu_{\text{max},a}}{(S_{\text{NH}_x} + \kappa_{\text{NH}_x,a})(S_{\text{O}_2} + \kappa_{\text{O}_2,a})} \quad (69)$$

$$d_h(X_h) := X_h \beta_h \quad (70)$$

$$d_a(X_a) := X_a \beta_a \quad (71)$$

$$a_N(S_{\text{bN}}, X_h) := S_{\text{bN}} X_h \lambda_{\text{am}} \quad (72)$$

$$h_o(S_{\text{NO}_x}, S_{\text{O}_2}, X_{\text{cb}}, X_h) := X_{\text{cb}} \lambda_{\text{hyd},b} \frac{X_h}{X_{\text{cb}} + X_h \kappa_{X_{\text{hyd}}}} \left( \frac{S_{\text{NO}_x} \eta_{\text{hyd},\text{an}} \kappa_{\text{O}_2,h}}{(S_{\text{NO}_x} + \kappa_{\text{NO}_x,h})(S_{\text{O}_2} + \kappa_{\text{O}_2,h})} + \frac{S_{\text{O}_2}}{S_{\text{O}_2} + \kappa_{\text{O}_2,h}} \right) \quad (73)$$

$$h_{\text{oN}}(S_{\text{NO}_x}, S_{\text{O}_2}, X_{\text{cbN}}, X_{\text{cb}}, X_h) := X_{\text{cbN}} \lambda_{\text{hyd},b} \frac{X_h}{X_{\text{cb}} + X_h \kappa_{X_{\text{hyd}}}} \left( \frac{S_{\text{NO}_x} \eta_{\text{hyd},\text{an}} \kappa_{\text{O}_2,h}}{(S_{\text{NO}_x} + \kappa_{\text{NO}_x,h})(S_{\text{O}_2} + \kappa_{\text{O}_2,h})} + \frac{S_{\text{O}_2}}{S_{\text{O}_2} + \kappa_{\text{O}_2,h}} \right) \quad (74)$$

$$(75)$$

$$\dot{S}_b := g_{\text{hAn}} m_{S_b} g_{\text{hAn}} + g_{\text{hO}_2} m_{S_b} g_{\text{hO}_2} + h_o \quad (76)$$

$$\dot{X}_{\text{cb}} := d_a m_{X_{\text{cb}}} d_a + d_h m_{X_{\text{cb}}} d_h - h_o \quad (77)$$

$$\dot{X}_h := -d_h + g_{\text{hAn}} + g_{\text{hO}_2} \quad (78)$$

$$\dot{X}_a := -d_a + g_{\text{aO}_2} \quad (79)$$

$$\dot{S}_{\text{O}_2} := g_{\text{aO}_2} m_{S_{\text{O}_2}} g_{\text{aO}_2} + g_{\text{hO}_2} m_{S_{\text{O}_2}} g_{\text{hO}_2} \quad (80)$$

$$\dot{S}_{\text{NO}_x} := g_{\text{aO}_2} m_{S_{\text{NO}_x}} g_{\text{aO}_2} + g_{\text{hAn}} m_{S_{\text{NO}_x}} g_{\text{hAn}} \quad (81)$$

$$\dot{S}_{\text{NH}_x} := a_N + g_{\text{aO}_2} m_{S_{\text{NH}_x}} g_{\text{aO}_2} + g_{\text{hAn}} m_{S_{\text{NH}_x}} g_{\text{hAn}} + g_{\text{hO}_2} m_{S_{\text{NH}_x}} g_{\text{hO}_2} \quad (82)$$

$$\dot{S}_{\text{bN}} := -a_N + h_{\text{oN}} \quad (83)$$

$$\dot{X}_{\text{cbN}} := d_a m_{X_{\text{cbN}}} d_a + d_h m_{X_{\text{cbN}}} d_h - h_{\text{oN}} \quad (84)$$

$$(85)$$

$$\dot{X}_{\text{nb},e} := d_a m_{X_{\text{nb},e}} d_a + d_h m_{X_{\text{nb},e}} d_h \quad (86)$$

$$\dot{S}_{\text{alk}} := a_N m_{S_{\text{alk}}} a_N + g_{\text{aO}_2} m_{S_{\text{alk}}} g_{\text{aO}_2} + g_{\text{hAn}} m_{S_{\text{alk}}} g_{\text{hAn}} + g_{\text{hO}_2} m_{S_{\text{alk}}} g_{\text{hO}_2} \quad (87)$$

$$\dot{S}_{\text{N}_2} := g_{\text{hAn}} m_{S_{\text{N}_2}} g_{\text{hAn}} \quad (88)$$

$$(89)$$

$$\dot{S}_{\text{nb}} := 0 \quad (90)$$

$$\dot{X}_{\text{nb},\text{in}} := 0 \quad (91)$$

$$(92)$$

This work	Other name	Value	Units	Description
$M_N$	$M_N$	14.0	$\text{g mol}^{-1}$	atomic molar mass of nitrogen
$\text{COD}_C$	$\text{COD}_C$	32.0	$\text{g mol}^{-1}$	Theoretical COD of molar carbon
$\text{COD}_{\text{Fe}}$	$\text{COD}_{\text{Fe}}$	24.0	$\text{g mol}^{-1}$	Theoretical COD of molar iron
$\text{COD}_H$	$\text{COD}_H$	8.0	$\text{g mol}^{-1}$	Theoretical COD of molar hydrogen
$\text{COD}_N$	$\text{COD}_N$	-24.0	$\text{g mol}^{-1}$	Theoretical COD of molar nitrogen
$\text{COD}_O$	$\text{COD}_O$	-16.0	$\text{g mol}^{-1}$	Theoretical COD of molar oxygen
$\text{COD}_P$	$\text{COD}_P$	40.0	$\text{g mol}^{-1}$	Theoretical COD of molar phosphorus
$\text{COD}_S$	$\text{COD}_S$	48.0	$\text{g mol}^{-1}$	Theoretical COD of molar sulphur
$\text{COD}_+$	$\text{COD}_{\text{pos}}$	-8.0	$\text{g mol}^{-1}$	Theoretical COD of positive charge
$\text{COD}_-$	$\text{COD}_{\text{neg}}$	8.0	$\text{g mol}^{-1}$	Theoretical COD of negative charge
$\beta_a$	$b_{\text{ANO}}$	0.15	$\text{d}^{-1}$	Decay rate for XANO ( $b_A$ )
$\beta_h$	$b_{\text{OHO}}$	0.62	$\text{d}^{-1}$	Decay rate for XOHO ( $b_H$ )
$\eta_{\text{an,h}}$	$n_{\text{mOHOAx}}$	0.8	-	Reduction factor for anoxic growth of XOHO ( $\eta_g$ )
$\eta_{\text{hyd,an}}$	$n_{\text{qhydAx}}$	0.4	-	Correction factor for hydrolysis under anoxic conditions ( $\eta_h$ )
$\gamma_a$	$Y_{\text{ANO}}$	0.24	$\text{g g}^{-1}$	Yield of XANO growth per SNO3 ( $Y_A$ )
$\gamma_h$	$Y_{\text{OHO}}$	0.67	$\text{g g}^{-1}$	Yield for XOHO growth ( $Y_H$ )
$i_{\text{COD,N2}}$	$i_{\text{CODN2}}$	$\text{COD}_N/M_N$	$\text{g g}^{-1}$	Conversion factor for N2 in COD ( $i_{\text{CODN2}}$ )
$i_{\text{COD,NO3}}$	$i_{\text{CODNO3}}$	$(\text{COD}_N + 3\text{COD}_O + \text{COD}_-)/M_N$	$\text{g g}^{-1}$	Conversion factor for NO3 in COD ( $i_{\text{CODNO3}}$ )
$i_{\text{NO3,N2}}$	$i_{\text{NO3N2}}$	$(-3\text{COD}_O - \text{COD}_-)/M_N$	$\text{g g}^{-1}$	Conversion factor for NO3 reduction to N2 ( $i_{\text{NO3N2}}$ )
$i_{\text{NXb}}$	$i_{\text{NXBio}}$	0.086	$\text{g g}^{-1}$	N content of biomass, meaning XOHO, XPAO, and XANO ( $i_{\text{XB}}$ )
$i_{\text{NXnb}}$	$i_{\text{NXUE}}$	0.06	$\text{g g}^{-1}$	N content of products from biomass ( $i_{\text{XE}}$ )
$i_{\text{cSNHx}}$	$i_{\text{ChargeSNHx}}$	$1/M_N$	$\text{mol g}^{-1}$	Conversion factor for NHx in charge ( $i_{\text{ChargeSNHx}}$ )
$i_{\text{cSNOx}}$	$i_{\text{ChargeSNOx}}$	$-1/M_N$	$\text{mol g}^{-1}$	Conversion factor for NO3 in charge ( $i_{\text{ChargeSNOx}}$ )
$\kappa_b$	$K_{\text{SBOHO}}$	20.0	$\text{g m}^{-3}$	Half-saturation coefficient for SB ( $K_S$ )
$\kappa_{\text{NHx,a}}$	$K_{\text{NHxANO}}$	1.0	$\text{g m}^{-3}$	Half-saturation coefficient for SNHx for XANO ( $K_{\text{NH}}$ )
$\kappa_{\text{NHx,h}}$	$K_{\text{NHxOHO}}$	0.05	$\text{g m}^{-3}$	Half-saturation coefficient for NH4 (not in classic ASM1)
$\kappa_{\text{NOx,h}}$	$K_{\text{NOxOHO}}$	0.5	$\text{g m}^{-3}$	Half-saturation coefficient for SNOx XOHO ( $K_{\text{NO}}$ )
$\kappa_{\text{O2,a}}$	$K_{\text{O2ANO}}$	0.4	$\text{g m}^{-3}$	Half-saturation coefficient for SO2 for XANO ( $K_{\text{OA}}$ )
$\kappa_{\text{O2,h}}$	$K_{\text{O2OHO}}$	0.2	$\text{g m}^{-3}$	Half-saturation coefficient for SO2 XOHO ( $K_{\text{OH}}$ )
$\kappa_{\text{Xhyd}}$	$K_{\text{XCBhyd}}$	0.03	$\text{g g}^{-1}$	Saturation coefficient for XB/XOHO ( $K_X$ )
$\lambda_{\text{am}}$	$q_{\text{am}}$	0.08	$\text{m}^3 \text{d}^{-1} \text{g}^{-1}$	Rate constant for ammonification ( $k_a$ )
$\lambda_{\text{hyd,b}}$	$q_{\text{XCBSBhyd}}$	3.0	$\text{g g}^{-1}$	Maximum specific hydrolysis rate of particulate and soluble biodegradable organics ( $k_h$ )
$\mu_{\text{max,h}}$	$m_{\text{OHOMax}}$	6.0	$\text{d}^{-1}$	Maximum growth rate of XOHO ( $\mu_H$ )
$\mu_{\text{max,a}}$	$m_{\text{ANOMax}}$	0.8	$\text{d}^{-1}$	Maximum growth rate of XANO ( $\mu_A$ )
$\zeta_{\text{Xnb,l}}$	$f_{\text{XUBiols}}$	0.08	$\text{g g}^{-1}$	Fraction of XU generated in biomass decay ( $f_P$ )

Table 4: Parameters

State variable	min	reference	max	reference
$S_b$	0.9	reactor 5 (Alex et al., 2008)	69	(Alex et al., 2008)
$S_{O_2}$	2	(Schneider et al., 2019)	2.2	(Schneider et al., 2019)
$X_{cb}$	49	reactor 5 (Alex et al., 2008)	82	reactor 1 (Alex et al., 2008)
$S_{NHx}$	1.7	reactor 5 (Alex et al., 2008)	8	reactor 1 (Alex et al., 2008)
$S_{NOx}$	6	reactor 1 (Alex et al., 2008)	10	reactor 5 (Alex et al., 2008)
$X_{cbN}$	0.01	reactor 1 (Alex et al., 2008)	3.5	reactor 5 (Alex et al., 2008)
$S_{bN}$	0.7	reactor 5 (Alex et al., 2008)	2	reactor 1 (Alex et al., 2008)
$X_h$	2304	reactor 5 (Alex et al., 2008)	2816	reactor 1 (Alex et al., 2008)
$X_a$	135	reactor 5 (Alex et al., 2008)	165	reactor 1 (Alex et al., 2008)

Table 5: Scenario 1 for range of concentrations in the reactor that the wastewater treatment process is designed for. Most values are taken from the [BSM1](#) (Alex et al., 2008). The dissolved oxygen  $S_{O_2}$  concentration is an exception as the model is not for a sequencing batch reactor and we used the values that we observed in an sequencing batch reactor. With this selection method  $X_h$  and  $X_a$  have the same value which is not suitable for our approach. Hence we took for the maximum +10% and for the minimum -10% from the value in the [BSM1](#) which are 2560 respectively 150.

State variable	min	reference	max	reference
$S_b$	0	-	2560	(Racho and Pongampornnara, 2020)
$S_{O_2}$	0	-	8	saturation concentration
$X_{cb}$	0.2	effluent (Alex et al., 2008)	91	mean of reactor 1 and underflow (Alex et al., 2008)
$S_{NHx}$	0	-	400	assumption based on (Dockhorn et al., 2014)
$S_{NOx}$	0	-	400	assumption based on (Dockhorn et al., 2014)
$X_{cbN}$	0.01	effluent (Alex et al., 2008)	6.5	mean of reactor 1 and underflow (Alex et al., 2008)
$S_{bN}$	0.7	reference	320	(How et al., 2020)
$X_h$	10	effluent (Alex et al., 2008)	3780	mean of reactor 1 and underflow (Alex et al., 2008)
$X_a$	0.6	effluent (Alex et al., 2008)	225	mean of reactor 1 and underflow (Alex et al., 2008)

Table 6: Scenario 2 for range of concentrations in the reactor which could happen in for example on-site wastewater treatment facilities. The assumption based on [Dockhorn et al. \(2014\)](#) is made that all nitrogen produces per day is present as NHx respectively NOx and that 60 liters of water are consumed per day.

State variable	min	reference	max	reference
$S_b$	0	-	8200	observed maximum(Lowe et al., 2009)
$S_{O_2}$	0	-	8	saturation concentration
$X_{cb}$	0	-	100	underflow (Alex et al., 2008)
$S_{NHx}$	0	-	300000	saturation concentration
$S_{NOx}$	0	-	9000	fertiliser production (Dhamole et al., 2007)
$X_{cbN}$	0	-	7	underflow (Alex et al., 2008)
$S_{bN}$	0	-	320	(How et al., 2020)
$X_h$	0	-	5000	underflow (Alex et al., 2008)
$X_a$	0	-	300	underflow (Alex et al., 2008)

Table 7: Scenario 3 for range of concentrations in the reactor which are physically possible, though many probably unlikely to happen.

## C Causal diagram

Confounding situations are when one sees an association (correlation) but there is no causal relationship. A mediator  $M$  ( $X \rightarrow M \rightarrow F$ ) might be present or the situation is spurious ( $X \leftarrow F \rightarrow Y$ ), which means that there is no causal relation that leads to the correlation between the two elements  $X$  and  $Y$ . Another situation in causal diagrams is a collider ( $X \rightarrow F \leftarrow Y$ ), which is also called a V-structure or immorality and is the structure that we observed between the different states of the [ASM1](#) and the [ramp](#) feature. The V-structure means that not only the variable of interest  $X$  leads to feature  $F$  ( $S_{NHx} < \text{threshold}$ ), but also several other state variables such as  $Y$ .

### C.1 Ammonium depletion soft-sensor based on the dissolved oxygen ramp feature

In a previous study (Schneider et al., 2019), the soft sensor for a maintained dissolved oxygen sensor reached a 93% accuracy with the **ramp** feature for a balanced dataset where half of the data had an ammonium concentration below or equal to a threshold  $T$  and half the data was above. The arbitrary threshold was chosen as double the amount of the detection limit of the ammonium measurements in the laboratory (i.e.  $1 \text{ g m}^{-3}$ ). For the unmaintained sensor, it was 80%. A high prediction accuracy could be achieved despite our study exposing alternative causes for the ramp.

In the previous study, we chose the most challenging real-world cases to which we were granted access. Additionally, we used synthetic, modelled data to make the feature fail to validate the feature and still obtained a wide range with high prediction accuracy (Schneider et al., 2020).

Nevertheless, despite the rigour that we used, the results of the **DSA** in this article clearly advise caution when barely deciding on fit in data-matching if a prediction is good enough or not. Especially in the face of climate change or on-site applications where conditions outside the training data set are likely to occur. This supports the statement by Zhong et al. who show the power of data-driven tools, but also caution that they should not be overly trusted either. **DSA** hence should indeed be applied much more frequently to decide if a feature is really robust or needs to be further refined or combined with other features, as the **ramp** feature will have to be.